

# PPAK Wide-field Integral Field Spectroscopy of NGC 628: I. The largest spectroscopic mosaic on a single galaxy<sup>\*</sup>

S. F. Sánchez,<sup>1</sup>† F. F. Rosales-Ortega,<sup>2</sup> R. C. Kennicutt,<sup>2</sup> B. D. Johnson,<sup>2</sup>  
A. I. Diaz,<sup>3</sup> A. Pasquali,<sup>4</sup> C. N. Hao<sup>2</sup>

<sup>1</sup>Centro Astronómico Hispano Alemán, Calar Alto, (CSIC-MPG), C/Jesús Durbán Remón 2-2, E-04004 Almeria, Spain

<sup>2</sup>Institute of Astronomy, Cambridge University, Madingley Road, Cambridge CB3 0HA, UK

<sup>3</sup>Departamento de Física Teórica, C-XI, Universidad Autónoma de Madrid, 28049 Madrid, Spain

<sup>4</sup>Max-Planck-Institut für Astronomie, Königstuhl 17, D-69117 Heidelberg, Germany

To be edited letter (June 2009)

## ABSTRACT

We present a wide-field IFS survey on the nearby face-on Sbc galaxy NGC 628, comprising 11094 individual spectra, covering a nearly circular field-of-view of  $\sim 6$  arcmin in diameter, with a sampling of  $\sim 2.7$  arcsec per spectrum in the optical wavelength range (3700–7000 Å). This galaxy is part of the PPAK IFS Nearby Galaxies Survey, (PINGS, Rosales-Ortega et al. 2009). To our knowledge, this is the widest spectroscopic survey ever made in a single nearby galaxy. A detailed flux calibration was applied, granting a spectrophotometric accuracy of  $\sim 0.2$  mag. The spectroscopic data was analysed both as a single integrated spectrum that characterises the global properties of the galaxy, and using each individual spectrum to determine the spatial variation of the stellar and ionized gas components. The spatial distribution of the luminosity-weighted ages and metallicities of the stellar populations was analysed. Using typical strong emission line ratios we derived the integrated and 2D spatial distribution of the ionized gas, the dust content, SFR, and oxygen abundance.

The age of the stellar populations shows a negative gradient from the inner (older) to the outer (younger) regions. We found an inversion of this gradient in the central  $\sim 1$  kpc region, where a somewhat younger stellar population is present within a ring at this radius. This structure is associated with a circumnuclear star-forming region at  $\sim 500$  pc, also found in similar spiral galaxies. From the study of the integrated and spatially resolved ionized gas we found a moderate SFR of  $\sim 2.4 M_{\odot} \text{ yr}^{-1}$ . The oxygen abundance shows a clear gradient of higher metallicity values from the inner part to the outer part of the galaxy, with a mean value of  $12 + \log(\text{O}/\text{H}) \sim 8.7$ . At some specific regions of the galaxy, the spatially resolved distribution of the physical properties show some level of structure, suggesting real point-to-point variations within an individual H II region. Our results are consistent with an inside-out growth scheme, with stronger star formation at the outer regions, and with evolved stellar populations in the inner ones.

**Key words:** techniques: spectroscopic – galaxies: individual: NGC 628 (M74) – galaxies: abundances – stars: formation – galaxies: ISM – galaxies: stellar content

## 1 INTRODUCTION

Galaxies in the local universe ( $\sim 10$  Mpc) are the fundamental anchor points of any study of the evolution of these objects in cosmological time scales. Therefore, it is important to understand their main properties, including their morphology, ionized and neutral gas content, stellar populations and metallicities. Due to their apparent scale-length they represent the perfect laboratories to study the depen-

<sup>\*</sup> Based on observations collected at the Centro Astronómico Hispano Alemán (CAHA) at Calar Alto, operated jointly by the Max-Planck Institut für Astronomie and the Instituto de Astrofísica de Andalucía (CSIC).

† E-mail: sanchez@cefca.es

dence of the stellar population, the star formation history, and star formation rate on the morphology and morphological substructures, the metallicity enrichment and the mechanisms of metal transfer, as well as the nature of the gas ionization.

Powerful constraints on theories of galactic chemical evolution, on the star formation history, and on the nucleosynthesis in galaxies can be derived from the accurate determination of the nature of the ionization, the star-formation rate and the chemical abundances at different locations within a galaxy. Fortunately, these sort of studies can be addressed using ground-based astronomy by observing galaxies with large apparent scale-lengths. Nearby galaxies may be more easily separated into a number of different morphological components and several types of stellar populations. Given the spatial variation in the star-formation histories (including violent episodes in some cases), and the amount of dust attenuation within a galaxy, and their relatively low surface brightness, it is difficult to study the stellar populations of nearby galaxies using just their integrated light. More information can be extracted by studying their resolved properties, although it is a complex task to tackle.

Nearby galaxies have been observed for many decades using many different techniques, such as multi-band optical and near-infrared broad-band imaging (to derive the properties of their dominant stellar populations and population gradients), narrow-band imaging and multi-object observations to derive their gas content and gas kinematics (e.g. Kennicutt & Hodge 1980; Belley & Roy 1992; Scowen et al. 1996), and slit spectroscopy of the brightest HII regions within the galaxy (e.g. McCall et al. 1985; Zaritsky et al. 1994; van Zee et al. 1998). More recent studies, using space-based observatories, have revealed new features in these apparently well known objects, such as star-forming regions at very large radii (e.g. GALEX Gil de Paz et al. 2007a,b) and obscured star-forming regions (e.g. Kennicutt et al. 2003; Prescott et al. 2007, SPITZER).

Despite all these efforts, we still lack of a complete picture of the main properties of these galaxies, especially those ones that can only be revealed by spectroscopic studies (like the nature of the ionization and/or the metal content of the gas). This is because previous spectroscopic studies only sample a very few discrete regions in these complex targets (e.g. Roy & Walsh 1988; Kennicutt & Garnett 1996), and in many cases they were sampling very particular types of regions (HII regions, McCall et al. 1985; van Zee et al. 1998; Castellanos et al. 2002b,a). Integrated spectra over large apertures are required to derive these properties in a more complete way, but are difficult to obtain using classical slit spectroscopy (although recent efforts have obtained integrated spectra of some local galaxies by adopting a drift-scan procedure (Moustakas & Kennicutt 2006b)). Even in these cases, only a single integrated spectrum is derived, and the spatial information is lost.

Recent studies have derived the integrated and spatially resolved properties of certain portions of nearby galaxies, by using Integral Field Spectroscopy (IFS) techniques (e.g. SAURON, Bacon et al. 2001; de Zeeuw et al. 2002). This technique allows one to obtain spatially resolved, continuously sampled spectroscopy over the field-of-view (FOV) of the instrument. These studies, though leading to extremely important results, were focused on the study of the cen-

tral regions of galaxies, with a FOV of radius  $\sim 20$  arcsec, corresponding on average to the inner  $\sim 1$  kpc. More recently, Blanc et al. (2009) observed the central region of M 51 ( $\sim 1.7$  arcmin<sup>2</sup>) using the VIRUS-P instrument. However, to date there has been no systematic study of a sample of local universe galaxies using IFS, covering a substantial fraction of their optical sizes.

In order to fill this gap, we began an IFS survey of 17 nearby ( $< 100$  Mpc) galaxies, called PINGS (PPAK Integral-field-spectroscopy Nearby Galaxies Survey, Rosales-Ortega et al. 2010, hereafter Paper I). By their nature, most of the objects in the survey cannot be covered in a single pointing with IFS instruments, and a new observing-reduction technique had to be developed to perform accurate mosaicking of the targets. In this article we present the first scientific results based on one of our targets, NGC 628 (or M 74). This is a local universe galaxy at  $z \sim 0.00219$  ( $\sim 9$  Mpc), and the largest in projected angular size of the PINGS sample.

In this first article of the series devoted to the IFS study of NGC 628, we present a study of the small and intermediate scale variation in the line emission and stellar continuum of NGC 628. We derive these properties from both the integrated spectrum of the galaxy and the spatially resolved spectra (by means of pixel-resolved maps across the disk of the galaxy), and compare the results. Additionally, we include a description of the data acquisition and reduction techniques, in particular on those details that are different than the standard reduction of IFS data and that were not addressed in Paper I. The structure of the article is as follows: In Section 2 we give an overview of the general properties of NGC 628. In Section 3 we present the observational details, including the instrument, telescope and the observing technique. In Section 4, we explain the reduction technique, describing the software packages used, and the sanity checks performed. In Section 5, we describe the analysis performed on each spectrum included in our dataset and consider also the integrated spectrum of the galaxy. The spatial distributions of the different derived properties are also presented here. In Section 6 we discuss the results and summarise the main conclusions of this study. Finally, in Appendix A, we describe in detail the technique used to analyse the stellar populations in the galaxy, including simulations to characterize its reliability.

## 2 GENERAL PROPERTIES OF NGC 628

Morphologically classified as an Sbc (Holmberg 1975), NGC 628 is a nearly face-on spiral, showing a typical grand-design structure. This galaxy has been well observed at a variety of wavelengths and there is abundant multi-wavelength ancillary data from photographic plates and CCD imaging in the optical (e.g. Holmberg 1975; Boroson 1981; Shostak & van der Kruit 1984; Natali et al. 1992; Hoopes et al. 2001; Kennicutt et al. 2008) to SPITZER in the NIR (SINGS, Kennicutt et al. 2003), and GALEX in the UV (Gil de Paz et al. 2007a). NGC 628 is a good example of an isolated galaxy, previous studies have established that NGC 628 has not had an encounter with satellites or other galaxies in the last  $10^9$  yr. (Kamphuis & Briggs 1992). However, it is possible that the galaxy suffered some kind

of interaction 1 Gyr ago, which could explain the presence of a large-scale oval structure (weak bar) discovered in the NIR (James & Seigar 1999; Seigar 2002), and the disturbed morphology in the north part of the galaxy.

By means of observations in neutral hydrogen, an elliptical ring-like structure was discovered well beyond the optical disc, at around 12 arcmin from the nucleus of the galaxy (Roberts 1962; Briggs et al. 1980), lying on a plane with  $\sim 15^\circ$  inclination with respect to the inner disc. The presence of this warped velocity field is a puzzle, given the apparent isolation of the galaxy which would rule out its origin by tidal disruption. However, this feature is most likely the result of the interaction with two large high-velocity clouds accreting onto the outer parts of the disc (Kamphuis & Briggs 1992; López-Corredoira et al. 2002; Beckman et al. 2003).

From the morphological and dynamical point of view, NGC 628 displays one prominent spiral arm to the south, and one or several disturbed spiral arms to the north (although UV observations have shown spiral arms with a more symmetrical appearance than in the optical), an inner rapidly rotating disc-like structure (Daigle et al. 2006), a CO-discovered circumnuclear ring of star formation at  $\sim 2$  kpc from the centre (Wakker & Adler 1995; James & Seigar 1999) thought to be the result of a barred potential (Seigar 2002), and a nuclear (nested) bar on a  $\sim 100$  pc scale (Laine et al. 2002). All these ingredients seem to suggest that the evolution of the structure in NGC 628 has been driven by secular evolution of the disc (Kormendy & Kennicutt 2004).

On the other hand, Cornett et al. (1994) found that the star formation history in NGC 628 varies with galactocentric distance (with a young stellar population in the circumnuclear region), while Natali et al. (1992) suggested a scenario with an inner and an outer disc with different stellar populations, with a transition region located at 8-10 kpc from the centre, the same radius at which Cepa & Beckman (1990) found that the star formation efficiency is at its minimum, which they interpreted as the corotation radius for the spiral arms.

More recently, Fathi et al. 2007 (hereafter Fathi07) presented a detailed kinematic analysis of the galaxy based on wide-field 2D Fabry-Perot maps of  $H\alpha$ . They found that the velocity dispersion of the gas and for individual H II regions is practically constant at all galactocentric distances covered by their study. This result, together with the fact that they were not able to distinguish true diffuse gas emission given that the star formation is widely distributed within the disc, let Fathi07 to suggest that the emission in  $H\alpha$  from the H II regions dominates any emission from the diffuse component. Furthermore, they confirmed the presence of a disc-like central structure, which they argue could have been built up by inflow from large galactocentric distances, suggesting that NGC 628 is in the process of forming a secular pseudo-bulge.

NGC 628 has been also a classical target for optical spectroscopy, there is a good spectroscopic coverage of many of its structures, from the core (Moustakas & Kennicutt 2006b) to many H II regions located within and beyond the optical disc of the galaxy (e.g. McCall et al. 1985; van Zee et al. 1998; Ferguson et al. 1998; Castellanos et al. 2002b). Integral field spectroscopy of the central core ( $\sim 33$  arcsec $\times$ 41 arcsec) of NGC 628 has been recently obtained

using the SAURON Integral Field Unit (Ganda et al. 2006, 2007). These studies showed that the stellar component rotates in the same direction as the gas, that the stellar velocity dispersion drops in the central zones (suggesting a dynamical cold inner disc), and that the  $H\beta$  distribution is more extended than the [O III] distribution, both suggesting a ring-like structure, confirming the 15-20 arcsec nuclear ring previously reported by Wakker & Adler (1995).

In terms of studies focusing on the gas-phase of the galaxy, and on particular on the determination of the chemical abundance of the galaxy, previous long-slit spectroscopic studies have derived the abundance gradient of NGC 628 up to relatively large galactocentric radii ( $\sim 2R_{25}$ ), using mainly empirical metallicity indicators based on the ratios of strong emission lines (e.g. McCall et al. 1985; Zaritsky et al. 1994; van Zee et al. 1998; Ferguson et al. 1998; Castellanos et al. 2002b). These studies have shown a higher metallicity content in the inner part of the galaxy, that the slope of the gradient is constant across the range of galactocentric distances sampled by the different studies, and that the oxygen abundance decrease is relatively small. In the dynamical scenario previously described, this allows a moderate mixing of the disc material driven by the large-scale oval distortion (Zaritsky et al. 1994). However, these results have been drawn from relatively few spectroscopically observed H II regions.

An alternative method was developed by Belley & Roy (1992), who derived reddenings,  $H\beta$  equivalent widths, diagnostic line ratios and metallicities for 130 H II regions by the implementation of imaging spectrophotometry, i.e. using narrow-band interference filters with the bandpass centered on several key nebular lines. They found no trends in the reddening nor for the  $H\beta$  EW's with galactocentric distance. However they found that the excitation, and some diagnostic line ratios are strongly correlated with galactocentric radius. They also derived an oxygen abundance gradient of NGC 628 based on the [O III]/ $H\beta$  ratio.

In summary, NGC 628 represents an interesting object for a full 2D spectroscopic study, considering that it is the prototype of a normal, isolated, grand-design, face-on, nearby spiral, with an interesting morphology and particular dynamical features. Furthermore, despite all the previous studies towards a full understanding of NGC 628, we still lack a detailed knowledge of the gas chemistry, stellar populations and the global properties across the surface of this galaxy, which can be only obtained by spectroscopic means. The IFS data presented in this and future papers aim to fill this gap, by deriving and comparing the global and spatially resolved spectroscopic properties of NGC 628 with previous results obtained by multi-wavelength observations. The information provided by these 2D spectral maps will allow us to test, confirm, and extend the previous body of results from small-sample studies, and would provide a new path for the analysis of the two-dimensional metallicity structure of disks and the intrinsic dispersion in metallicity on this and other late-type normal spirals.

### 3 OBSERVATIONS

Observations were carried out at the 3.5m telescope of the Calar Alto observatory with the Potsdam Multi Aperture

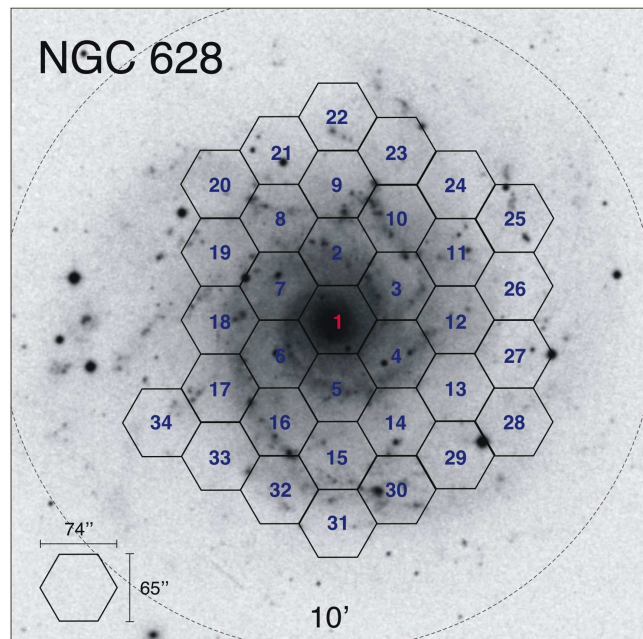


**Figure 1.** *B*-band Digital Sky Survey image of NGC 628. The mosaic of the PPAK pointings is shown as overlaid hexagons indicating the field-of-view of the central fibre-bundle. The identification number of each pointing is indicated, as listed in Table 1. The circle indicates the  $D_{25}$  radius (in the *B*-band). The image is  $10' \times 10'$  and it is displayed in top-north, left-east standard configuration.

Spectrograph, PMAS, (Roth et al. 2005) in the PPAK mode (Verheijen et al. 2004; Kelz et al. 2006). The PPAK fibre bundle consists of 382 fibres of 2.7 arcsec diameter each (see Fig. 5 in Kelz et al. 2006). Of these 382 fibres, 331 (the science fibres) are concentrated in a single hexagonal bundle covering a field-of-view of  $72'' \times 64''$ , with a filling factor of  $\sim 65\%$ . The sky background is sampled by 36 additional fibres, distributed in 6 bundles of 6 fibres each, distributed along a circle  $\sim 90$  arcsec from the center of the instrument FOV. The sky-fibres are distributed among the science fibres within the pseudo-slit in order to have a good characterization of the sky; the remaining 15 fibres are used for calibration purposes. Cross-talk between adjacent fibres is estimated to be less than 5% when using a pure aperture extraction (Sánchez 2006). Adjacent fibres in the pseudo-slit may come from very different locations on the spatial plane (Kelz et al. 2006), minimizing the effect of the cross-talk even more (although it does introduce an incoherent contamination not important for the present study).

The V300 grating was used for all the observations, covering the wavelength range  $\sim 3700$ - $7100$  Å, with a spectral resolution of  $FWHM \sim 8$  Å. Due to the large size of NGC 628 ( $\sim 10.5 \times 9.5$  arcsec) compared to the FOV of the instrument a mosaicking scheme was adopted, following the experiment by Sánchez et al. (2007b) using the same instrument. The initial pointing was centered on the centre of the galaxy. Consecutive pointings followed an hexagonal pattern, adjusted to the shape of the PPAK science bundle. Each pointing centre is 60 arcsec distant from the previous pointing centre. Due to the shape of the PPAK bundle and by construction of the mosaic 11 spectra of each pointing,

**Table 1.** Log of the observations.

Date	Pointings
28/10/06	1,2,3,9,10,22,23
10/12/07	1,4,5,6,7,8
11/12/07	14,15,16,17,18,19,30
12/12/07	11,12,13,25,29,31,32
09/08/08	11
30/10/08	24,26,27,28,29,33,34

corresponding to one edge of the hexagon, overlap with the same number of spectra from the previous pointing. This pattern was selected to maximise the covered area, minimise large gaps, and allow enough overlap of fibres to calibrate exposures taken under different atmospheric conditions. For the central pointing we adopted a dithering scheme with three positions having offsets  $(0'', 0'')$ ,  $(+0.78'', +1.68'')$ , and  $(+0.78'', -1.68'')$  following Sánchez et al. (2007c). This dither pattern allows us to cover the gaps between fibres and to increase the spatial resolution in this region (where more structure is expected). For each non-dithered pointing we obtained 3 exposures of 600s each, and for the central, dithered, pointings we obtained 2 exposures of 600s each.

The observations spanned six nights, distributed over three different years. In Fig. 1 the field-of-view of each pointing, labelled with its corresponding identification number, is overlaid on top of a *B*-band Digital Sky Survey<sup>1</sup> Note that a substantial fraction of the galaxy is covered by the IFS mosaic. Table 1 gives a log of the observations, including the date of observation and the pointings observed each night, following the identification numbers shown in Fig. 1. A concentric observing sequence was adopted, starting from the inner to the outer regions. The atmospheric conditions varied between the different observing runs, although in general they were clear but non-photometric. The seeing varied between  $\sim 1$  and  $\sim 1.8$  arcsec and the median of the seeing over all nights was  $\sim 1.4$  arcsec. Different spectrophotometric stars were observed during the observing runs, with at least two stars observed each night, in order to perform flux calibration. In addition to the science pointings, sky exposures of 300s were taken each night in order to perform a proper subtraction of the sky contribution. Additional details on the observing strategy can be found in Paper I.

## 4 DATA REDUCTION

Data reduction was performed using R3D (Sánchez 2006), in combination with IRAF<sup>2</sup> packages and E3D (Sánchez

<sup>1</sup> The Digitized Sky Survey was produced at the Space Telescope Science Institute under U.S. Government grant NAG W-2166. The images of these surveys are based on photographic data obtained using the Oschin Schmidt Telescope on Palomar Mountain and the UK Schmidt Telescope. The plates were processed into the present compressed digital form with the permission of these institutions.

<sup>2</sup> IRAF is distributed by the National Optical Astronomy Observatories, which are operated by the Association of Universities for Research in Astronomy, Inc., under cooperative agreement with the National Science Foundation.

2004). The reduction consists of the standard steps for fibre-based integral-field spectroscopy. A master bias frame was created by averaging all the bias frames observed during the night and subtracted from the science frames. The different exposures taken at the same position on the sky were then combined, clipping the cosmic rays, using IRAF routines. Then the locations of the spectra on the CCD were determined using a continuum illuminated exposure taken before the science exposures. Each spectrum was then extracted from the science frames. In order to reduce the effects of the cross-talk we did not perform a simple aperture extraction, which would consist of co-adding the flux within a certain number of pixels of location derived from the continuum illuminated exposure. Instead, we adopted a modified version of the Gaussian-suppression technique described in Sánchez (2006).

The new technique assumes a Gaussian profile for the projection of each fibre spectrum along the cross-dispersion axis. It basically performs a Gaussian fitting to each of the fibres after subtracting the contribution of the adjacent fibres in an iterative process. First, a simple aperture extraction is performed with a 5 pixel aperture. This initial guess of the flux corresponding to each spectrum is then used to model the profiles with a Gaussian function, adopting as centroid the location of the peak intensity determined from the continuum exposure. The width of the model Gaussian is taken from the average width of all the fibre profiles ( $\sigma \sim 2$  pixels). In this first iteration the aperture extracted flux is used as the integrated flux of the Gaussian function. This modelled profile is then used, for each spectrum, to remove the contribution of the four adjacent fibre spectra. The resulting *clean* profile is then fitted with a Gaussian function, with the centroid and width parameters fixed, in order to derive a better estimation of the integrated flux. This new flux is used as the input for the next iteration of the process. It was found that with three iterations the procedure converges, increasing the signal-to-noise ratio of the extracted spectra and reducing the effect of cross-talk.

The extracted flux, for each pixel in the dispersion direction, is stored in a row-stacked-spectrum file RSS (Sánchez 2004). Wavelength calibration was performed using HeHgCd lamp exposures obtained before and after each pointing, yielding an accuracy of  $rms \sim 0.3$  Å. Differences in the relative fibre-to-fibre transmission throughput were corrected by comparing the wavelength-calibrated RSS science frames with the corresponding frames derived from sky exposures taken during the twilight.

Although PPAK is equipped with fibres to sample the sky, in most of our pointings the sky fibres are located within an area containing significant signal from the galaxy. Accurate sky subtraction was therefore an important issue in the data reduction. For the different nights and pointings we adopted different sky subtraction schemes depending on the position of the pointing. In some cases, a sufficient number of sky-fibres are located in regions free from galaxy emission, and it was possible to perform an accurate sky subtraction of the individual pointings using these sky spectra. Once a certain frame is properly sky-subtracted, the sky spectrum of any adjacent frame, observed in the same night and under similar weather conditions, can be easily estimated. To do so the spectra of the 11 fibres in the sky subtracted frame that overlap an adjacent frame (that has not been sky subtracted)

are combined. This combined spectrum is then subtracted from the corresponding combined spectrum of the 11 fibres of the adjacent frame. This produces an estimation of the sky spectrum in the adjacent frame that is then subtracted from all the spectra in that frame. Prior to this subtraction it is necessary to visually check that no residual of the galaxy is kept in the estimated sky spectrum, which can occur if the atmospheric transmission changed substantially between the observations of the two frames.

In other frames the sky observations taken during the night could be used to subtract the sky in the science observations, especially when the sky and target exposures are taken within a few minutes of each other. When the exposures were more widely separated in time it was necessary to combine different sky frames with different weights to derive good results. The criterion adopted to decide when a subtraction was good or not was to minimise the residuals in the typical emission features of the night spectrum. A thorough analysis of the sky subtraction and the residuals found in the reduction of this galaxy can be found in Paper I.

After reducing each individual pointing we built a single RSS file for the mosaic following an iterative procedure. The spectra of each pointing were scaled to those of the previous pointing by the average ratio in the 11 overlapping spectra. Those overlapping spectra were then replaced by the average between the previous pointing and the new rescaled spectra. The resulting spectra were incorporated into the final RSS file, updating the corresponding position table. By adopting this procedure the differences in the spectrophotometric calibration night-to-night and frame-to-frame are normalized to that of the first frame used in the process. For this reason the mosaic was constructed starting from the central frame observed in the night of the 10th of December 2007, under nearly photometric conditions according to the Calar Alto extinction monitor. The final mosaic dataset comprises 11094 non-overlapping individual spectra, covering a field-of-view of  $\sim 6' \times 7'$ , i.e.  $\sim 70\%$  of the optical size of the galaxy (defined by  $D_{25}$  mag arcsec $^{-2}$  radius in the  $B$ -band), and therefore represents the largest spectroscopic survey of a single galaxy.

#### 4.1 Accuracy of the flux calibration

Although particular care has been taken to achieve the best spectrophotometric calibration, there many effects that can strongly affect it. Among them, the most obvious are the photon-noise from low surface brightness regions of the galaxy, the sky-background noise or variations in the weather conditions between the time when the spectrophotometric standards and the object were observed. This latter effect was reduced by the adopted mosaicking procedure in the data reduction, since the photometric calibration was renormalized to that of a particularly good night. Less obvious is the effect of inaccuracies in the sky subtraction. However, for low surface brightness regions this is one of the most important effects.

Since it is our goal to provide accurate spectrophotometric data, we performed a flux re-calibration on the data. To do so we used the flux calibrated broad-band optical images from the SINGS legacy survey (Kennicutt et al. 2003). In particular, we compared our dataset with the  $B$ ,  $V$ ,  $R$  and  $H\alpha$  images, since they are mostly covered by the wavelength

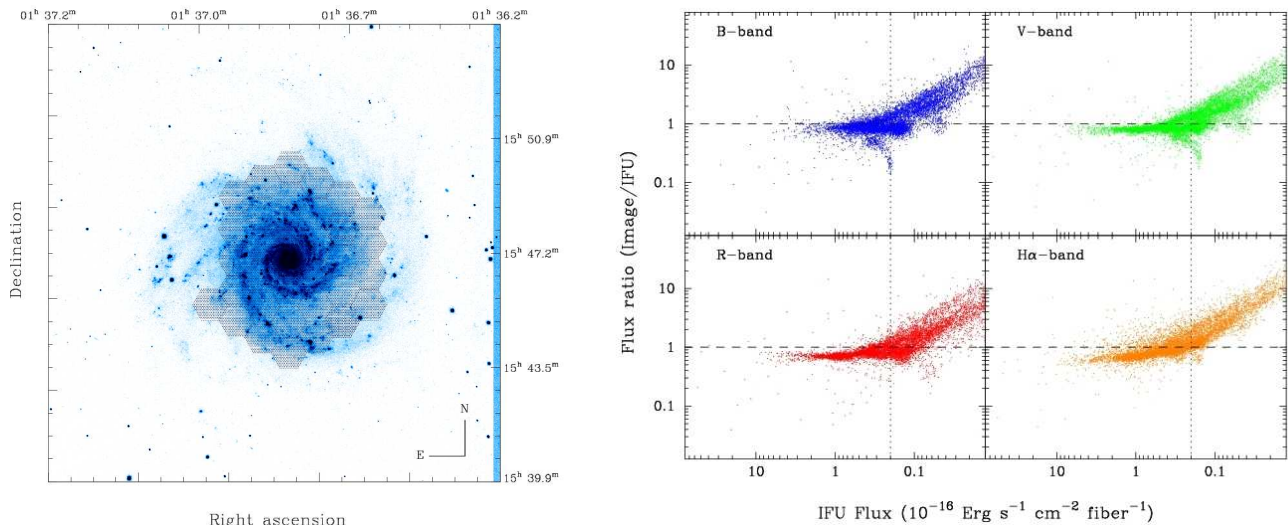


**Figure 2.** Left: SINGS *B*-band image of NGC 628 used to perform the absolute flux re-calibration. The position of each fibre of the IFS mosaic is shown overlaid to the real scale. Right: Distribution of the ratio between the flux in the apertures corresponding to the PPAK fibres on each of the flux-calibrated broad-band images obtained from the SINGS ancillary data and the corresponding flux extracted from the IFU data. Each panel shows the results for the different imaging data: *B*-band (top-left panel), *V*-band (top-right panel), *R*-band (bottom-left) and  $H\alpha$  (bottom-right panel). The horizontal dashed-line indicate the one-to-one ratio, which the vertical dotted-line indicate the adopted intensity cut for acceptable flux calibration.

range of our spectra. The photometric calibration of those images is claimed to be  $\sim 5\%$  for the broad-band images and  $\sim 10\%$  for the narrow-band images. They reach a depth of  $\sim 25$  mag/arcsec<sup>2</sup> with a signal-to-noise of  $\sim 10\sigma$ . Therefore, for the structures included in the FOV of our IFS data, the photometric errors of the imaging are dominated by the accuracy of the calibration, and not by the photon-noise.

The IFS mosaic was registered to the SINGS optical data by matching the coordinates of the galaxy bulge and foreground stars in the FOV (see the left-panel of Fig. 2). After this process the error in the astrometry of the IFS data was estimated to be  $\sim 0.3''$ , based on the *rms* of the differences in the centroid of the stars and galaxy bulge. Once registered, the mosaic position table was used to extract aperture photometry from each broad-band image at the location of each fibre and with an aperture similar to that of the fibres. The photometry was transformed to flux (in cgs units) by using the counts-to-magnitude prescription in the SINGS documentation<sup>3</sup>, and the zero-points included in Fukugita et al. (1995). On the other hand, each spectrum in the mosaic was convolved with the corresponding transmission curve of the filters indicated before, in order to extract a similar flux fibre-to-fibre, based on the IFS data. This procedure provides us with 11094 photometric points per band to compare between the two datasets.

The right-panel of Fig. 2 shows the ratio between the two sets of photometric points versus the flux extracted from the IFU data, for each of the considered filters. The figure shows the typical pattern obtained when comparing the flux ratio between two datasets with different depth, with the broad-band images clearly deeper than the spectroscopic data, as expected. Down to  $0.2 \cdot 10^{-16}$  erg s<sup>-1</sup> cm<sup>-2</sup> ( $\sim 5772$  fibres) the ratio is  $\sim 0.9$  for all the fibres, with a standard

deviation of  $\sim 0.3$  dex. Small differences in the transmission curves of the filters used in this calculation and the ones used by Fukugita et al. (1995) as well as the astrometric errors described before introduce uncertainties in the derived fluxes which increase the standard deviation. The uncertainties from the former source are difficult to estimate. However the uncertainties introduced by astrometric errors are estimated to be at least  $\sim 10\%$ , by simulating different mosaic patterns, moving the location of fibres randomly within 0.3 arcsec (the uncertainty of our astrometry) and comparing the extracted photometry. Based on all these results we estimate our spectrophotometric accuracy to be better than  $\sim 0.2$  mag when we apply the re-calibration derived by this flux ratio analysis. The overall re-normalization factor applied to the IFS mosaic was 1.15, derived as the average of the ratios found on each band. This difference in the zero-point of the flux calibration lies within the expectations based on the estimated accuracy of our spectrophotometric calibration.

Fig. 3 shows in the left-panel, the comparison between the drift-scan spectrum of the central region of NGC 628 (blue line), published by Kennicutt et al. (2003)<sup>4</sup>, and the integrated spectrum extracted from the spectrophotometrically re-calibrated PINGS mosaic (black line), after co-adding the spectra within a simulated aperture with the same size, location and PA as the SINGS drift-scan. The SINGS drift-scan corresponds to a  $20''$  aperture and  $70^\circ$  PA. The right-panel of Fig. 3 shows a  $100 \text{ \AA}$  width narrow-band map of the mosaic of NGC 628 centered at  $H\alpha$ , the red box in the centre corresponds to the simulated aperture from which the IFS spectrum was extracted. The coordinates, size and PA of the aperture were obtained from the header of the SINGS data file. Some gaps in between the edges of

<sup>3</sup> <http://tinyurl.com/SINGS-doc>

<sup>4</sup> <http://irsa.ipac.caltech.edu/data/SPITZER/SINGS/galaxies/ngc0628.html>

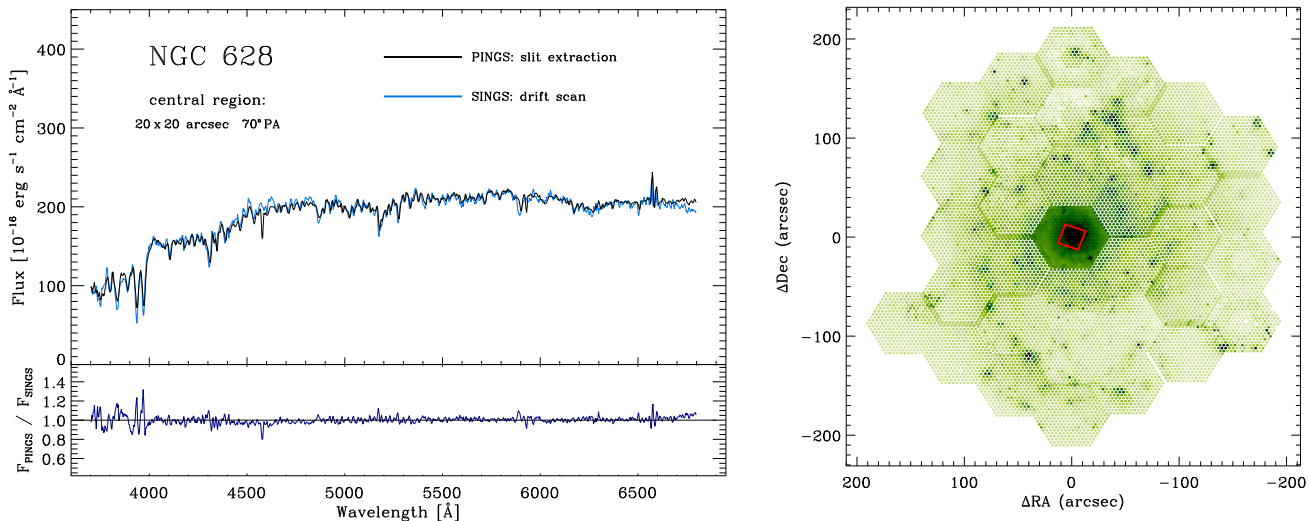


**Figure 3.** Left: Comparison between the spectrum extracted for the central region of NGC 628 (shown in the right-panel) using the PPAK data (black-line) after co-adding the spectra within a simulated aperture with the same size, location and PA as the SINGS legacy survey drift-scan (blue-line, in the online version of the paper). The bottom-panel shows the ratio between the two spectra. Right: Narrow-band map of the PINGS mosaic of NGC 628 centered at H $\alpha$ , the red box in the centre corresponds to the simulated aperture from which the IFS spectrum was extracted. Despite the different techniques used to derive both spectra, there is a clear agreement between them in most of the wavelength range.

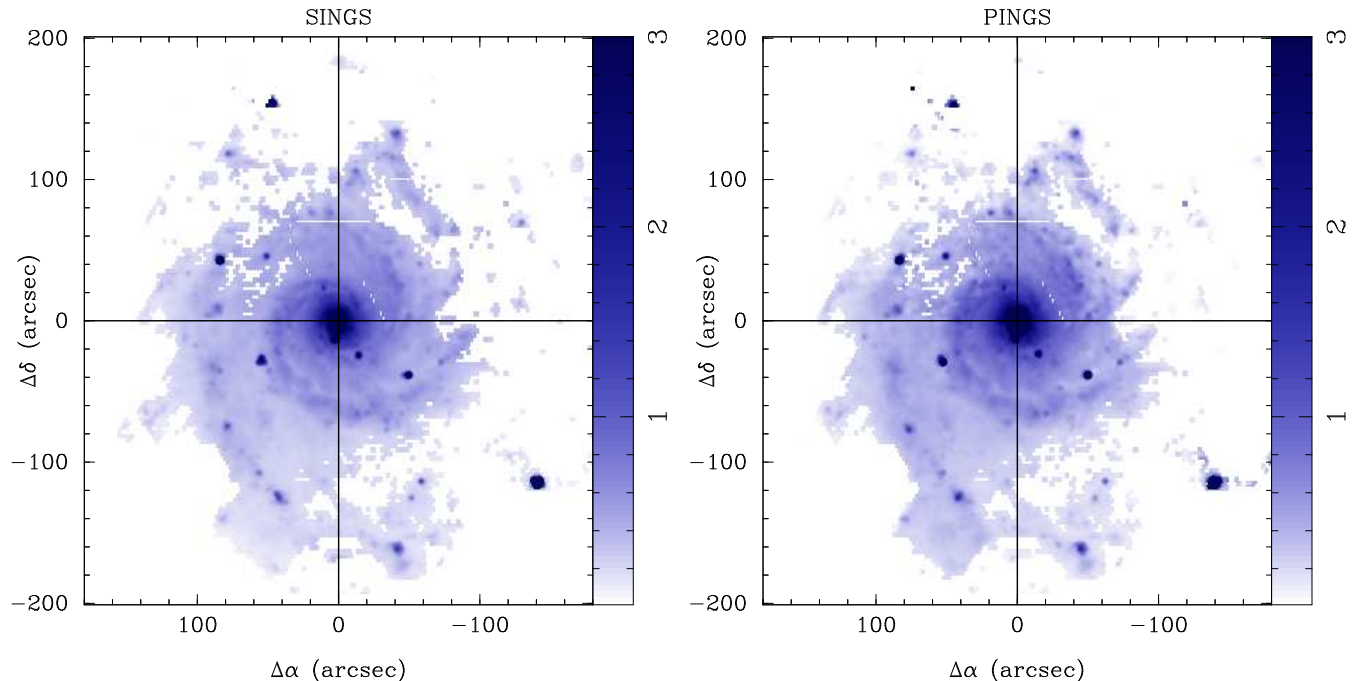
the pointings are seen in this map, they are due to the re-centering of the individual pointings after comparing with the broad-band images as discussed in above. As expected from the spectrophotometric re-calibration of the mosaic, there is a very good agreement between both datasets; both the general shape of the spectra and the strength of the spectral features match well. The left-panel of Fig. 3 shows in the lower part the relative difference between the two spectra, which is consistent with a null difference (in average) and within the error of the absolute flux calibration for most of the spectral range. As simulations with different position, apertures and mosaic versions showed, the small deviations in the continuum are due to the presence of a foreground star within the FOV of the simulated slit. The small disagreement at wavelengths shorter than 4000 Å is expected due to the degradation of the CCD sensitivity in the blue, as explained in detailed in Paper I, where further comparisons with previous spectrophotometric data can be found. A slight mismatch of the wavelength resolution at the edges of the spectra is also noticed, being in the range of the expectations for such comparisons.

Fig. 4 shows the comparison between two reconstructed V-band images of NGC 628. The image on the left was created after interpolating the aperture photometry extraction of the SINGS broad-band image. The image on the right was derived from the flux re-calibrated IFS dataset, once each spectrum corresponding to a particular fibre was convolved with the filter response, as described before. In order to create a regularly gridded image, the data were interpolated using E3D (Sánchez 2004), adopting a natural-neighbor non-linear interpolation scheme, and a final pixel scale of 1''/pixel. The areas not fulfilling our criteria for accurate spectrophotometry ( $F_V < 0.210 \cdot 10^{-16}$  erg s<sup>-1</sup> cm<sup>-2</sup>) were masked.

## 5 ANALYSIS AND RESULTS

In order to extract physical properties of the galaxy from the dataset it is necessary to perform different kinds of analyses. In particular, for each spectrum we need to identify the emission lines of ionized gas, and decouple this emission from the underlying stellar population. Particular care has to be taken in this decoupling technique, since some of the emission lines (e.g. H $\beta$ ) may be strongly affected by underlying absorption features.

The decoupling of the stellar population from the emission lines was performed adopting a scheme summarized here: (i) A set of detected emission lines was identified in the integrated spectra of the stronger H II regions in the outer part of the galaxy. (ii) For each spectrum in the dataset, the underlying stellar population was fitted by a linear combination of a grid of single-stellar population (SSP) templates, after correcting for the appropriate systemic velocity and velocity dispersion (including the instrumental dispersion which dominates the total observed dispersion), and taking into account the effects of dust attenuation. A spectral region of 30 Å width around each detected emission line was masked prior to the linear fitting, including also the regions around the sky-lines (Sánchez et al. 2007a). (iii) Once we derived a first approximation of the spectrum of the underlying stellar population, this was subtracted from the original spectrum to obtain a pure emission-line spectrum. (iv) To derive the intensity of each detected emission line, each of these *clean* spectra in the dataset was fitted to a single Gaussian function per emission line plus a low order polynomial function. Instead of fitting emission lines over the entire wavelength range simultaneously, for each spectrum we extracted shorter wavelength ranges that sampled one or a few of the analysed emission lines, in order to characterise



**Figure 4.** Reconstructed  $V$ -band images of NGC 628. Left: image created after interpolating the aperture photometry extraction of the SINGS broad-band image. Right: interpolated image derived after multiplying each spectrum of the IFS mosaic with the filter response curve. Both images were created with a regular grid of  $1''$ /pixel. The areas not satisfying our criteria of accurate spectrophotometry were masked. The perpendicular lines are centered at the mosaic’s reference point. Offsets are in arcsec.

the residual continuum with a simple polynomial function, and to simplify the fitting procedure. When more than one emission line was fitted simultaneously, their systemic velocities and FWHMs were forced to be equal (since the FWHM is dominated by the instrument resolution), in order to decrease the number of free parameters and increase the accuracy of the deblending process (when required). (v) Finally, for each spectrum in the dataset a pure gas-emission spectrum was created, based on the results of the last fitting procedure, using only the combination of Gaussian functions. This model was then subtracted from the original data, spectrum by spectrum, to produce a dataset of gas-free spectra. These spectra are then fitted again by a combination of SSP, as described before (but without masking the spectral range around the emission lines, in this case), deriving the *luminosity-weighted* age, metallicity and dust content of the composite stellar population. The Appendix A gives a detailed description of the fitting procedure, indicating the basic algorithms adopted, and including estimates of the accuracy of the SSP-based modeling and the derived parameters based on simulations. The 2D maps of the emission line intensities and physical properties shown in the following sections were constructed based on the pure gas-emission mosaics described above.

### 5.1 Integrated spectrum

A particularly interesting use of IFS datasets is the combination of the observed spectra to produce an integrated spectrum of the object, using the IFU as large aperture spectrograph. This high signal-to-noise integrated spectrum can be used to derive, for the first time, the real average spectroscopic properties of the galaxy, as opposed to previous stud-

ies that attempted to describe its average properties by the analysis of individual spectra taken at different regions. The most similar approach would be the spectrum derived by using a drift-scanning technique (e.g. Moustakas & Kennicutt (2006b) and part of the ancillary data of the SINGS survey), although in those studies (specially for the latter) the fraction of galaxy covered by the spectra was much less than for the spectrum presented here. Another advantage of the use of an IFU with respect to the drift-scan technique is that the former allows a comparison between the integrated and the spatially resolved properties of the galaxy.

A good amount of the fibres in the IFS mosaic of NGC 628 do not contain enough signal-to-noise or do not contain signal at all (i.e. spectra with a flat continuum consistent with zero-flux), as the fibres were sampling regions where the intrinsic flux from the galaxy is low or null (e.g. borders of the mosaic, intra-arms regions, etc). In order to get rid of spectra where no information could be derived, we obtained a *clean* version of the IFS mosaic of NGC 628 by applying a flux threshold cut choosing only those fibres with an average flux along the whole spectral range greater than  $10^{-16}$  erg s $^{-1}$  cm $^{-2}$  Å $^{-1}$ . Furthermore, bad fibres (due to cosmic rays and CCD cosmetic defects) and foreground stars (10 within the observed field-of-view of NGC 628) were removed from the mosaic. This procedure resulted in a refined mosaic version which includes only those regions with high-quality spectrophotometric calibration. The total number of spectra in the *clean* IFS mosaic version of NGC 628 is 6949. The top-panel of Fig. 5 shows the integrated spectrum of NGC 628 derived by co-adding the spectra within the *clean* IFS mosaic version of the galaxy.

The integrated spectrum of NGC 628 shows a characteristic stellar continuum with absorption features and emission

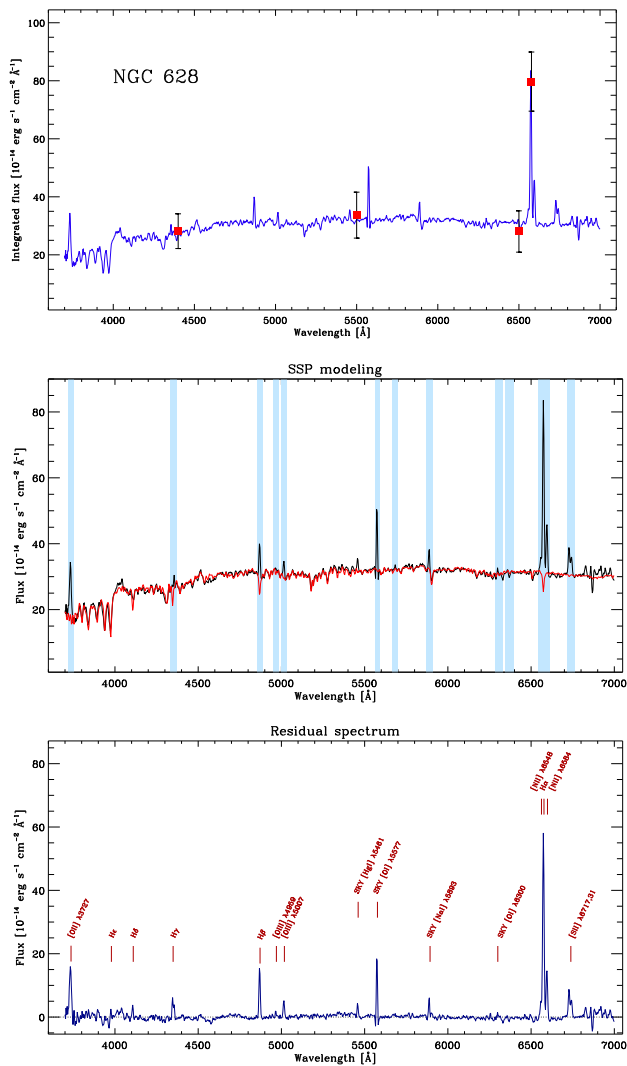


**Figure 5.** Integrated spectrum of NGC 628. The red solid squares in the top-panel indicate the integrated flux derived from the  $B$ ,  $V$ ,  $R$  and  $H\alpha$  images. The middle-panel shows the SSP model fitting (red-line, in the online version) to the spectrum, the light-blue bands correspond to the spectral regions masked during the fitting. The bottom panel shows the residual after subtracting the model from the original spectrum, the detected emission lines have been labeled.

lines superimposed.  $H\alpha$ ,  $H\beta$ , [O II]  $\lambda$ 3727, [O III]  $\lambda$ 5007, the [N II]  $\lambda$ 6548,84 and  $\lambda$ 6717,31 doublets are clearly identified. Less obvious are the  $H\gamma$  and [O III]  $\lambda$ 4959 lines. Sky residuals are also present in the spectrum, especially the [O I]  $\lambda$ 5577 and [Na I]  $\lambda$ 5893 lines. The red-solid squares (in the online version) correspond to the integrated flux derived from the  $B$ ,  $V$ ,  $R$  and  $H\alpha$  images of the SINGS ancillary data, obtained during the spectrophotometric re-calibration, using the same apertures of the IFU data and co-adding them in a similar way as the integrated spectrum. The position of these data-points with respect to the continuum (in the case of the broad-band images) and the peak of the  $H\alpha$  line in the spectrum, corroborates the accuracy of the absolute flux calibration. The co-added region comprises  $\sim 90\%$  of the total flux of the galaxy in  $V$ -band, as estimated from corresponding SINGS image. An analysis similar to that de-

scribed above was performed on this integrated spectrum to derive the main physical properties of both the ionized gas and the stellar population.

### 5.1.1 Integrated stellar populations

The middle-panel of Fig. 5 shows the best SSP model fit to the integrated spectrum superimposed in red colour. The light-blue bands correspond to the spectral regions masked during the fitting as explained above. They coincide with the position of the strongest redshifted emission lines and regions of bright sky residuals. Note the strength of the underlying stellar absorptions in the Balmer lines. The multi-component SSP model matches accurately the continuum of the integrated spectrum, within an error of the  $\sim 3\%$ . Most of the discrepancies are in regions clearly dominated by imperfections in the sky-subtraction, due to the strength of the night sky lines (e.g. at  $\sim \lambda$ 5577, see Sánchez et al. (2007a) and Paper I). In order to evaluate the possible effects of these residuals in the derivation of the main properties of the stellar population the analysis was repeated for the wavelength range between  $\lambda$ 4100 and  $\lambda$ 5400  $\text{\AA}$ , where there are no such strong atmospheric features. For this wavelength range, the model matches the continuum within a  $\sim 2\%$ . In the UV-regime the errors are sometimes larger than this value.

Table 2 lists the *luminosity-weighted* age, metallicity and dust attenuation of the best fitting model for the two cases considered here: one using the entire spectral range in the fitting process and the other using the reduced range described before. There is a very good agreement between the results derived in both cases. Based on the results from the simulations (see Appendix), we expect an error of 10-20% in the derivation of the Age, and of a  $\sim 5\%$  in the derivation of the metallicity. These errors do not take into account the systematics, due to the applied algorithm, the current code and the templates adopted, or the known degeneracies in the derivation of the age and the metallicity, and therefore the expected discrepancies with previous published results are much larger than the ones estimated on the basis of the simulations. From these fits we may conclude that the average stellar population of NGC 628 is dominated by an old component of  $\sim 9$  Gyrs, but with a subsolar metallicity ( $[Z/H] \sim -0.45$ ). Although synthesis modeling is nowadays widely used, we have to take into account the age-metallicity degeneracy problem that plagues most spectral fitting techniques. The most frequently used technique to derive the age and metallicity of the stellar population in galaxies is to measure certain line strength indices, such as the Lick/IDS index system (e.g. Burstein et al. 1984; Faber et al. 1985; Burstein et al. 1986; Gorgas et al. 1993; Worthey 1994). For this purpose, one generally tries to use a combination of indices that are most orthogonal in the parameter space (i.e. age and metallicity). In order to cross-check the results based on the fitting procedure, we measured the equivalent width of  $H\beta$  (primarily sensitive to the age) and  $Mgb$  (primarily sensitive to the metallicity), of the integrated spectrum.

The equivalent widths of the absorption lines were derived using the bandpass definitions from the Lick index system revised by Trager et al. (1998), shifted to the redshift of the object, as described in Sánchez et al. (2007c). To derive the age and metallicity from the measured indices, we

**Table 2.** Properties of the average stellar population.

Analysis method	Age (Gyr)	Metallicity		$A_{V,\star}$ (mag)
		Z	[Z/H]	
SSP fit, 3700-6800 Å	8.95	0.007	-0.44	0.4
SSP fit, 4100-5400 Å	8.40	0.007	-0.44	0.8
H $\beta$ vs. Mgb indices	9.78	0.008	-0.42	—

\* Dust continuum attenuation.

have adopted the model grid from Thomas et al. (2003), implemented in the RMODEL code<sup>5</sup>. The resulting estimates of the age and metallicity, based on the absorption line index analysis, are listed in Table 2. Despite the strong conceptual differences between these methods and the fitting technique described before, the results are very consistent with the values obtained in both the full and reduced wavelength range SSP fitting.

### 5.1.2 Integrated properties of the ionized gas

The bottom-panel of Fig. 5 shows the pure emission line spectrum of NGC 628 obtained after subtracting the underlying stellar population from the integrated spectrum. As expected, the spectrum is dominated by a set of emission lines, plus a residual continuum consistent with a zero average intensity. This procedure reveals additional emission lines, like H $\delta$  and H $\epsilon$ . All the detected lines have been labeled with their standard notation. Each of these emission lines was fitted with a single Gaussian function, as described before, in order to derive their strengths. Fig. 6 shows an example of the fits in the wavelength range between 6500 Å and 6800 Å. The black solid-line corresponds to the pure emission line spectrum of NGC 628, the red dashed-line shows the best fitted model, consisting of six Gaussian functions, assuming a single Gaussian fit to each of the emission lines detected in this wavelength range: the [N II] doublet, H $\alpha$ , He I  $\lambda$ 6678 (very faint) and the [S II] doublet. In this particular case both the systemic velocity and velocity dispersion were forced to be the same for all the emission lines, in order to increase the accuracy of the derived parameters. The ratio between the two [N II] lines included in the spectral range were fixed to the theoretical value (Osterbrock & Ferland 2006). A similar procedure was applied to the rest of the emission lines. By adopting this procedure, it is possible to accurately deblend the different emission lines.

Table 3 lists the emission line intensities derived using this procedure, including for each of the detected emission lines its standard identification, the laboratory rest-frame wavelength, and the estimated intensity normalised to the observed flux of H $\beta$  in units of  $10^{-15}$  erg s $^{-1}$  cm $^{-2}$ . They are shown in the columns labeled as  $F(\lambda)/H\beta$ . The observed [O III] ratio shown in Table 3 is consistent with the well-known theoretical value between these lines (Storey & Zeippen 2000). The associated  $1\sigma$  errors are solely due to the statistical uncertainty  $\sigma_{\text{stat}}$  in the measurement of the flux intensity. Thereafter, the observed line intensities were corrected for reddening using the Balmer decrement according to the reddening function of Cardelli et al.

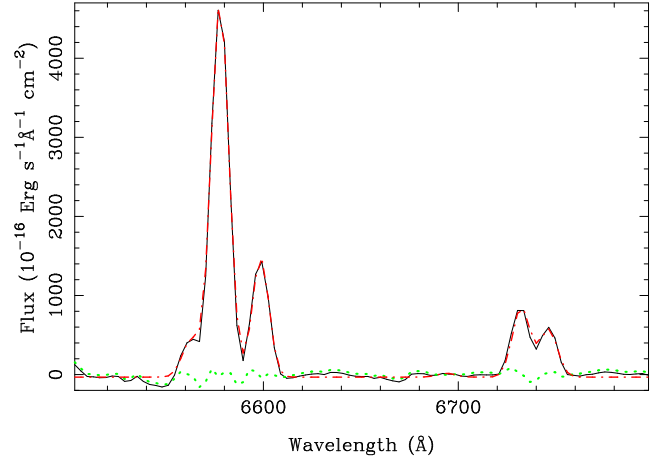


**Figure 6.** Example of the fitting procedure applied to derive the intensity flux of the detected emission lines. The black solid-line corresponds to the pure emission line spectrum of NGC 628, covering the wavelength range between 6500 and 6800 Å. The red dashed-line shows the best fitting model describing the emission lines, which comprises a single Gaussian function for each of them. The green dotted-line shows the residual spectrum, once the previous model has been subtracted.

**Table 3.** Integrated line intensities for NGC 628. The first column corresponds to the emission line identification, with the rest-frame wavelength, the second one corresponds to the adopted reddening curve normalized to H $\beta$ . The  $F(\lambda)/H\beta$  column corresponds to the observed flux, while the  $I(\lambda)/H\beta$  to the reddening corrected values; normalised to H $\beta$ . The values in parenthesis correspond to the  $1\sigma$  errors calculated as explained in the text. The observed flux in H $\beta$  is in units of  $10^{-15}$  erg s $^{-1}$  cm $^{-2}$ . The last row shows the number of fibres from which the integrated spectra was extracted.

Line	$f(\lambda)$	$F(\lambda)/H\beta$	$I(\lambda)/H\beta$
[O II] $\lambda$ 3727	0.32	1.494 (0.046)	2.138 (0.320)
H $\delta$ + He I $\lambda$ 3889	0.29	0.158 (0.032)	0.217 (0.054)
H $\delta$ $\lambda$ 4101	0.23	0.165 (0.032)	0.214 (0.051)
H $\gamma$ $\lambda$ 4340	0.16	0.511 (0.023)	0.609 (0.083)
H $\beta$ $\lambda$ 4861	0.00	1.000 (0.014)	1.000 (0.052)
[O III] $\lambda$ 4959	-0.03	0.111 (0.010)	0.108 (0.017)
[O III] $\lambda$ 5007	-0.04	0.329 (0.010)	0.315 (0.040)
He I $\lambda$ 5876	-0.20	0.299 (0.012)	0.239 (0.031)
[N II] $\lambda$ 6548	-0.30	0.383 (0.013)	0.276 (0.035)
H $\alpha$ $\lambda$ 6563	-0.30	3.998 (0.041)	2.870 (0.352)
[N II] $\lambda$ 6584	-0.30	1.111 (0.016)	0.795 (0.098)
[S II] $\lambda$ 6717	-0.32	0.619 (0.011)	0.435 (0.054)
[S II] $\lambda$ 6731	-0.32	0.393 (0.010)	0.276 (0.035)
[O III] $\lambda$ 5007/ $\lambda$ 4959		2.96 (0.28)	2.92 (0.58)
[S II] $\lambda$ 6717/ $\lambda$ 6731		1.57 (0.14)	1.58 (0.28)
F(H $\beta$ ) $\lambda$ 4861		1549.4	
c(H $\beta$ )		0.48 (0.05)	
$A_V$		1.04	
Extraction fibres		6949	

<sup>5</sup> N. Cardiel, <http://tinyurl.com/rmodel>

(1989), assuming  $R \equiv A_V/E(B - V) = 3.1$ . Theoretical values for the intrinsic Balmer line ratios were taken from Osterbrock & Ferland (2006), assuming case B recombination (optically thick in all the Lyman lines), an electron density of  $n_e = 100 \text{ cm}^{-3}$  and an electron temperature  $T_e = 10^4 \text{ K}$ . The last column of Table 3 shows the reddening-corrected emission line fluxes for the integrated spectrum, designated by  $I(\lambda)/H\beta$ . These flux ratios can be used to derive the average properties of the ionized gas in the galaxy. The adopted reddening curve normalized to  $H\beta$ ,  $f(\lambda)$ , is shown in the second column of the table. Although higher-order Balmer lines were detected in the integrated spectrum, no Balmer lines beyond  $H\gamma$  were used for the determination of  $c(H\beta)$ , as the associated error of the measurement of these lines in the residual spectrum yielded high uncertainties in the computed  $c(H\beta)$ , due to their low signal-to-noise; therefore the  $c(H\beta)$  value was derived using the  $H\alpha/H\beta$  ratio solely. No auroral lines were detected either in the integrated or residual spectrum. The low strength of the [O III] lines suggests a relatively high metallicity for the integrated abundance of NGC 628, as it will be shown hereafter.

Although particular care has been taken in the flux calibration of the spectra within the mosaic, the absolute flux intensity listed in Table 3 has to be treated with caution. On one hand, not all of the galaxy surface has been covered by our IFS observations, as can be seen in Fig. 1. In particular some of the brighter H II regions, located to the east of NGC 628 are not included in the FOV of our mosaic. This causes to underestimate the intensity of all the lines. By a rough estimation, based on the  $D_{25}$  optical radius ( $B$ -band), we consider that our IFS Mosaic covers  $\sim 70\%$  of the galaxy size. On the other hand, the central fibre-bundle of PPAK has a filling factor of  $\sim 65\%$ , as mentioned in Section 3, which leads to a corresponding underestimation of the integrated flux. In the particular case of this mosaic, a dithering scheme necessary to compensate for this incomplete sampling was adopted only for the central pointing, where the emission lines are in general weak. All together, we consider that it is necessary to apply a correction of a factor  $\sim 2.2$  to take into account the aperture and sampling effects described before. As mentioned before, NGC 628 has been extensively studied before in several publications. In particular, different authors have reported on the  $H\alpha$  intensity flux, using different procedures, from photoelectric photometers to narrow-band imaging. Table 4 lists a summary of these published values, together with the value derived from our integrated spectrum and considering the flux correction factor described above. Despite the different biases introduced by the different methods, there is substantial agreement between the previously published results and our reported value for the integrated  $H\alpha$  flux of the galaxy.

The derived dust extinction,  $A_V = 1.04$ , larger than the one derived from the analysis of the stellar populations ( $A_V \sim 0.4 \text{ mag}$ ). This result is not surprising, since both methods sample different regions of the galaxy. While the underlying continuum is dominated by the stellar components of the central regions, clearly brighter, the ionized gas spectrum is dominated by the star-forming regions in the spiral arms. These latter regions are known to be more attenuated by dust, due to star forming process (e.g. Calzetti 2001). Indeed, the extinction law derived by Calzetti (1997) for star-forming galaxies shows that the typical extinction in

**Table 4.** Comparison between different  $H\alpha$  fluxes reported for NGC 628 in the literature. Fluxes in units of  $10^{-11} \text{ erg s}^{-1} \text{ cm}^{-2}$ .

Flux	Reference
1.07	Kennicutt 1983
0.87	Young et al. 1996
1.51	Hoopes et al. 2001
1.05	Marcum et al. 2001
1.02	Kennicutt et al. 2008
1.14	Current study

the emission lines of these objects is approximately double that in their stellar continuum.

The integrated flux of  $H\alpha$  and [O II]  $\lambda 3727$  can be used to determine a rough value of the global star formation rate (SFR) in this galaxy. The intensities of both lines were corrected by dust extinction, adopting the  $A_V$  value and the aperture correction mentioned before. Absolute luminosities were derived by assuming a standard  $\Lambda$ CDM cosmology with  $H_0=70.4$ ,  $\Omega_m=0.268$  and  $\Omega_\Lambda=0.73$ , and a luminosity distance of 9.3 Mpc (Hendry et al. 2005). The derived luminosities are  $L_{H\alpha} \sim 3.08$  and  $L_{[\text{O II}]} \sim 2.30$ , in units of  $10^{41} \text{ erg s}^{-1}$ . The values of the SFR were derived adopting the classical relations by Kennicutt (1998), obtaining  $\text{SFR} \sim 2.4$  and  $3.2 M_\odot \text{ yr}^{-1}$ , based on the  $H\alpha$  and [O II] luminosities respectively.

Different possible mechanisms can be responsible for the ionization in emission line galaxies. The nature of the ionization can be derived from ratios of the usual diagnostic lines (BPT, Baldwin et al. 1981; Veilleux & Osterbrock 1987). Based on the values listed in Table 3, it was found that  $\log_{10}([\text{N II}] \lambda 6584/H\alpha) \sim -0.56$  and  $\log_{10}([\text{O III}] \lambda 5007/H\beta) \sim -0.5$ . These line ratios correspond to the expected values for star forming galaxies and/or H II regions (e.g. Sánchez et al. 2005, 2007c), far away from any of the boundary regions in the [O III] /  $H\beta$  vs. [N II] /  $H\alpha$  diagnostic diagram. Therefore, it is clear that the dominant ionization mechanism in the integrated spectrum of NGC 628 is due to hot OB stars (H II regions), as expected, since no previous study has reported any kind of nuclear activity in this galaxy.

The (volume-averaged) ionization parameter, defined as the ratio of the density of ionizing photons to the particle density:  $u = \frac{Q_{H^0}}{4\pi R_s^2 n c}$ , where  $Q_{H^0}$  is the flux of ionizing photons produced by the exciting stars above the Lyman limit,  $R_s$  is the radius of the Strmgren sphere,  $n$  the number density of hydrogen atoms, and  $c$  the speed of light. This parameter determines the degree of ionization at any particular location within the nebula. As discussed in the next section, many of the empirical methods commonly used to derive the chemical abundance of a star-forming region are sensitive to this parameter, and for some ranges of metallicity, they are not useful unless the ionization parameter can be constrained within a small range of possible values.

The ionization parameter is best determined using the ratios of emission lines of different ionization stages of the same element. In general, the larger the difference in ionization potentials of the two stages, the better the constrain. A

commonly used ionization parameter diagnostic is based on the ratio  $[\text{O II}]/[\text{O III}] = \lambda 3727 / (\lambda 4959 + \lambda 5007)$ . However, this ratio is not only sensitive to the ionization parameter, but is also strongly dependent on metallicity. Another possibility is to use the  $[\text{S III}] \lambda 9069$  and/or  $[\text{S III}] \lambda 9532$  together with the  $[\text{S II}] \lambda 6717, \lambda 6731$  emission lines. The  $[\text{S II}]/[\text{S III}]$  ratio provides a more reliable useful ionization parameter diagnostic (Díaz et al. 1991). Considering the available lines within the spectral range of the PINGS observations (Díaz 1994), a good approximation to the ionization parameter can be determined from the  $[\text{O II}]/\text{H}\beta$  or  $[\text{S II}]/\text{H}\alpha$  ratio, via:

$$\log u = -0.80 \log([\text{O II}]/[\text{O III}]) - 3.02, \quad (1)$$

after Díaz et al. (2000). Its uncertainty is estimated to be  $\pm 0.2$  dex. The derived  $\log u$  for integrated spectrum of NGC 628 is  $-3.58$ , which corresponds to a low value of the ionization parameter ( $\sim 10^{-4}$ ).

### 5.1.3 Integrated oxygen abundance

Galaxies in the local universe have been used as an anchor point to determine the evolution of the metallicity (based on the gas phase oxygen abundance), along different cosmological periods. The global metallicity of a given galaxy is represented by its oxygen abundance. The rest of the elements vary within the same fractions as those found in the Sun. However, while the determination of this observable at high redshift normally describes the average value of the galaxies as a whole (due to aperture effects), in the local universe most of these determinations are based on studies of a number of discrete H II regions. The integrated spectrum of NGC 628 can be used to perform an integrated abundance analysis in a consistent way as the studies performed over high redshift galaxies, with the advantage that the results of the integrated study can be compared with the abundances of resolved regions within the galaxy. In this section, we present a chemical abundance analysis of the integrated spectrum of NGC 628 based on a suite of different empirical abundance diagnostic methods. A more detailed comparison between the integrated and spatially resolved abundances will be presented in a subsequent paper (Rosales-Ortega et al., in preparation).

Given the limitations imposed by the non-detection of auroral temperature sensitive emission lines (such as  $[\text{O III}] \lambda 4363$  or  $[\text{N II}] \lambda 5755$ ) in H II regions of low-excitation and/or low surface brightness, empirical methods based on the use of strong, easily observable optical lines have been developed throughout the years. Although abundances derived in this way are recognised to suffer considerable uncertainties, they are believed to be able to trace large-scale trends in galaxies. Following these ideas, several abundance calibrators have been proposed involving different emission-line ratios and have been applied to determine oxygen abundances in objects as different as individual H II regions in spiral galaxies, dwarf irregular galaxies, nuclear starburst, and the integrated abundances of spiral galaxies (e.g. Kobulnicky et al. 1999; Pilyugin et al. 2004, and references therein).

In order to derive the characteristic chemical abundance of NGC 628, a set of empirical calibrators were applied to the integrated spectrum. Different abundance es-

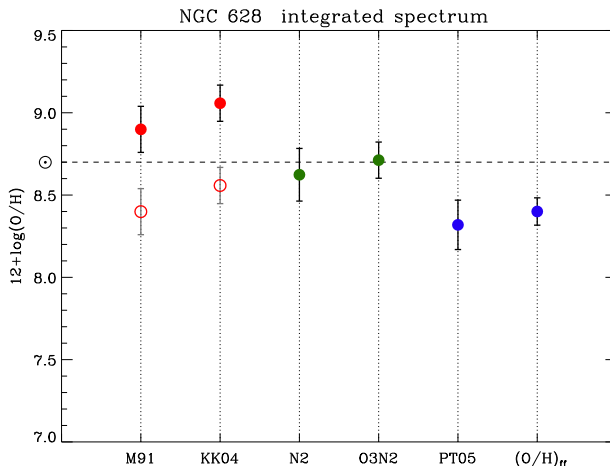


**Figure 7.** Comparison of the integrated oxygen abundance of NGC 628 derived for different estimators. Red-solid points correspond to  $R_{23}$  calibrators, green-points to index-empirical methods, and blue-points to the different methods proposed by Pilyugin and collaborators. The open circles correspond to an arbitrary  $-0.5$  dex offset of the  $R_{23}$  based methods. The horizontal dashed-line correspond to the oxygen solar value.

timators were chosen in order to explore the effect of a particular calibration depending on the physical properties of the galaxy. By far, the most commonly used such ratio is  $([\text{O II}] \lambda 3727 + [\text{O III}] \lambda 4959, \lambda 5007)/\text{H}\beta$ , known as the  $R_{23}$  method (Pagel et al. 1979). The logic for the use of this ratio is that it is not affected by differences in relative elemental abundances, and remains essentially constant within a given giant H II region despite variations in excitation (Díaz et al. 1987). However, there is an ambiguity inherent to this method since there are two values of abundance corresponding to a given value of  $R_{23}$ , i.e. the lower branch increases with increasing abundance, while the upper branch shows an opposite behavior, i.e.  $R_{23}$  decreases with increasing abundance. Another drawback of using  $R_{23}$  (and many of the other emission-line abundance diagnostics) is that it depends also on the ionization parameter. From this category, two methods were applied: the McGaugh 1991 (hereafter M91) and the Kobulnicky & Kewley 2004 (hereafter KK04) calibrations, which are theoretical methods based on photoionization models. Both take into account the ionization parameter to produce an estimate of the metallicity. The estimated accuracy of these methods is  $\sim \pm 0.15$  dex.

In order to discriminate between the different  $R_{23}$  branches, we used the  $[\text{N II}] \lambda 6584/[\text{O II}] \lambda 3727$  ratio following the prescriptions by Kewley & Dopita (2002). The  $[\text{N II}]/[\text{O II}]$  ratio is not sensitive to the ionization parameter to within  $\pm 0.05$  dex, and it is a strong function of metallicity above  $\log([\text{N II}]/[\text{O II}]) \gtrsim -1.2$ , where the division between the upper and lower branches occurs. The  $\log([\text{N II}]/[\text{O II}])$  value for the integrated spectrum of NGC 628 is  $-0.43$ , i.e. indicating that the  $R_{23}$  value of the integrated spectrum for NGC 628 ( $\log R_{23} = 0.41$ ) corresponds to the upper branch of the  $R_{23}$  relation.

Another subset of estimators was chosen from the category of empirical strong-line methods, they correspond to the N2 calibration (first proposed by Storchi-Bergmann et al. 1994, but using the definition af-

**Table 5.** Integrated oxygen abundances for NGC 628 in units of  $12 + \log(\text{O}/\text{H})$ . The columns designations correspond to the following abundance calibrators: M91, McGaugh (1991); KK04, Kobulnicky & Kewley (2004); N2, Denicoló et al. (2002); O3N2, Pettini & Pagel (2004); PT05, Pilyugin & Thuan (2005);  $(\text{O}/\text{H})_{\text{ff}}$ , ff- $T_e$  method (as explained in the text).

log $R_{23}$	M91	KK04	N2	O3N2	PT05	$(\text{O}/\text{H})_{\text{ff}}$
0.41	$8.90 \pm 0.14$	$9.06 \pm 0.11$	$8.62 \pm 0.16$	$8.71 \pm 0.11$	$8.32 \pm 0.15$	$8.55 \pm 0.09$

ter Denicoló et al. 2002), and the O3N2 calibration (first proposed by Alloin et al. (1979), but using the definition by Pettini & Pagel 2004). These two indices have the virtue of being single-valued, however, they are affected by the low-excitation line  $[\text{N II}] \lambda 6584$ , which may arise not only in bona-fide H II regions, but also in the diffuse ionized medium, which is an issue for spectra integrated within extended regions, such as the integrated spectrum of NGC 628. The estimated uncertainty of the derived metallicities is  $\sim \pm 0.2$  dex.

The Pilyugin & Thuan 2005 (hereafter PT05) calibration is based on an updated version of the Pilyugin (2001) estimator, obtained by empirical fits to the relationship between  $R_{23}$  and  $T_e$  metallicities for a sample of H II regions. This estimator was also considered to determine the integrated abundance of NGC 628. This calibration includes and excitation parameter  $P$  that takes into account the effect of the ionization parameter. The PT05 calibration has two parametrizations corresponding to the lower and upper branches of  $R_{23}$ . As in the case of the M91 and KK04 calibrators, the  $[\text{N II}]/[\text{O II}]$  ratio was used to discriminate between the two branches of the  $R_{23}$  relation.

The last strong-line empirical method considered is a combination of the flux-flux (or ff-relation) found by Pilyugin (2005) and parametrised by Pilyugin et al. (2006), the  $t_2 - t_3$  relation between the  $\text{O}^+$  and  $\text{O}^{++}$  zones electron temperatures for high-metallicity regions proposed by Pilyugin (2007), and an updated version of the  $T_e$ -based method for metallicity determination (Izotov et al. 2006). According to these authors, the combination of these methods solves the problem of the determination of the electron temperatures in high-metallicity H II regions, where faint auroral lines are not detected. However, the abundances determined through this method rely on the validity of the classic  $T_e$  method, which has been questioned for the high-metallicity regime in a number of studies by comparisons with H II region photoionization models (Stasińska 2005). The abundances derived through this method will be referred as  $(\text{O}/\text{H})_{\text{ff}}$  or ff- $T_e$  abundances.

The advantages and drawbacks of all these different calibrators have been thoroughly discussed in the literature (e.g. Pagel et al. 1980, Kennicutt & Garnett 1996, Kewley & Dopita 2002, Pérez-Montero & Díaz 2005, Kewley & Ellison 2008). Regrettably, comparisons among the metallicities estimated using these methods reveal large discrepancies. They are usually manifested as systematic offsets in metallicity estimates, with high values corresponding to theoretical calibrations and lower metallicities estimated by electron temperature metallicities, with offsets as large as 0.5 dex in  $\log(\text{O}/\text{H})$  units (Liang et al. 2006).

The calculated oxygen abundances (in units of  $12 + \log(\text{O}/\text{H})$ ) derived for each of the calibrators listed above are shown in Section 5.1.3. The uncertainties cor-

respond to the  $1\sigma$  error found by propagating the errors through a Monte Carlo simulation by using Gaussian distributions with a width equal to the errors of the emission line intensities, modulated by recomputing the distribution 500 times. These abundances are plotted in Fig. 7. The red-solid points (in the online version) correspond to the  $R_{23}$  methods, the green points to the index-empirical methods, and the blue points to the different methods proposed by Pilyugin and collaborators. The red-open circles correspond to an arbitrary  $-0.5$  dex offset of the  $R_{23}$  methods (these offsets are included given the well-known systematic offset of the  $R_{23}$  theoretical-based calibrations). The horizontal dotted-line corresponds to the oxygen solar abundance  $12 + \log(\text{O}/\text{H}) = 8.7$  (Scott et al. 2009).

The two  $R_{23}$  methods derive super-solar metallicity values, while the PT05 oxygen value correspond to the lowest metallicity obtained. The index-empirical methods, N2 and O3N2, stand in between the metallicities derived through the  $R_{23}$  and the PT05 + ff- $T_e$  methods. Interestingly, the  $R_{23}$  calibrations metallicities which were shifted to a lower value (red-open circles), are in close agreement (within the errors) to the pure-empirical and the ff- $T_e$  based metallicities. The mean oxygen abundance derived from all the methods is  $12 + \log(\text{O}/\text{H}) = 8.69 \pm 0.31$ .

Previous studies have determined the oxygen abundance in this galaxy based on spectroscopic imaging spectrophotometry observations of different H II regions. In particular, McCall et al. (1985) analysed a sample of H II regions within a radius of  $\sim 200$  arcsec, basically coincident with the area sampled by our IFS survey. They reported a range of oxygen abundances between  $12 + \log(\text{O}/\text{H}) \sim 8.7 - 9.3$  (by employing a method based on the  $R_{23}$  index), with a considerable decline from the inner to the outer parts. Belley & Roy (1992) obtained reddenings,  $\text{H}\beta$  equivalent widths, diagnostic line ratios and metallicities for 130 H II regions by the implementation of imaging spectrophotometry. They derived an abundance gradient of NGC 628 based on the  $[\text{O III}]/\text{H}\beta$  empirical calibrator (Edmunds & Pagel 1984). Their values range between  $12 + \log(\text{O}/\text{H}) \sim 8.4 - 9.2$ , covering a large baseline in galactocentric distances (up to  $\rho \sim 2\rho_{\text{eff}}$ ). Although this was not a strict spectroscopic study, given the number of H II regions analysed, the work of Belley & Roy 1992 stood up to now as the most complete 2D description of the emission line chemistry of NGC 628. Subsequently, van Zee et al. (1998) reported the oxygen abundances of the H II regions in an outer ring between  $\sim 150$  arcsec and  $\sim 300$  arcsec radius. They found that the decline in the abundance continues, and the oxygen abundance ranges between  $12 + \log(\text{O}/\text{H}) \sim 8.10$  and  $8.95$  (using a modified version of the M91 calibrator). More recently, Castellanos et al. (2002b) observed a reduced set of H II regions in the optical and near-infrared where they were able to measure temperature-sensitive emission lines. They re-

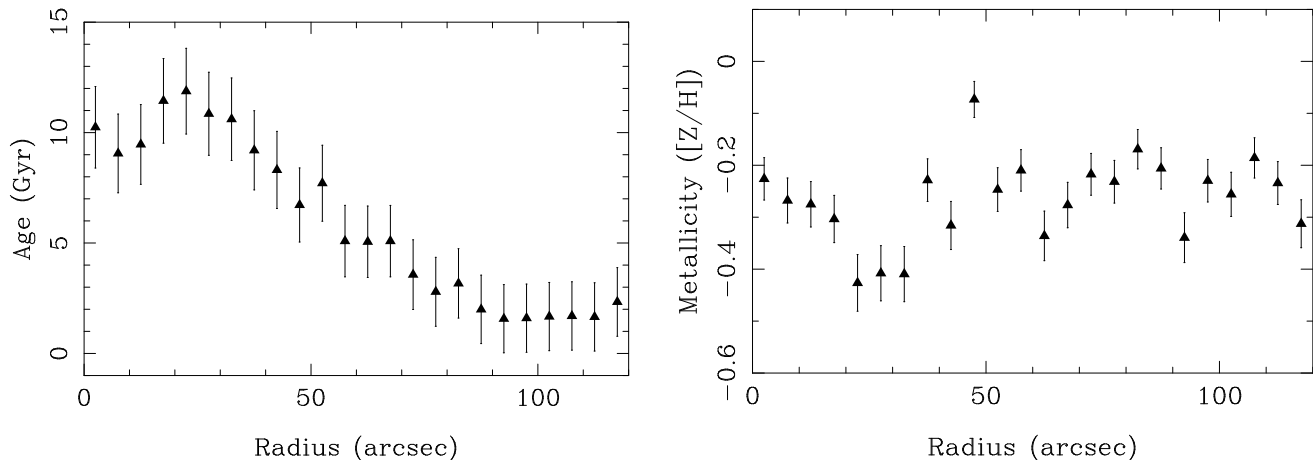


**Figure 8.** *Left panel:* radial distribution of the luminosity-weight age (in Gyr), of the stellar population based on the fitting procedure using the combination of multiple SSPs. *Right panel:* similar distribution for the luminosity-weight metallicity, relative to the solar one ( $Z/H$ ).

ported an average oxygen abundance of  $12 + \log(O/H) \sim 8.23$ . However these HII regions are located beyond the FOV of our IFS mosaic, at galactocentric distances where, given the well-known radial metallicity gradient of this galaxy (Ferguson et al. 1998), the oxygen abundance is expected to be lower than the integrated metallicity derived at inner radii. Therefore we cannot compare the integrated O/H abundance derived in this work with the values of Castellanos et al. (2002b) due to the non-coincident geometry. On the other hand, the range of oxygen abundances reported by the previous spectroscopic and imaging spectrophotometry studies agree perfectly with the integrated abundances derived through the  $R_{23}$  methods and with the mean integrated abundance of NGC 628.

The integrated properties of the ionized gas derived in this chapter need to be compared with the resolved properties in order to analyse the validity of the results obtained from the integrated analysis, taking into account different effects, such as the extinction or the contribution of the diffuse interstellar emission. These points will be addressed in the following sections.

## 5.2 Spatially resolved properties of the galaxy

In this section we present the results obtained by applying the spectra fitting technique described in Section 5 to each individual spectrum of the dataset. As indicated in the Appendix A, the technique allows the decoupling of the SED of the underlying stellar population from that of the ionized gas. This step is needed to derive the intensities of the different emission lines detected in each spectrum accurately. In addition, when the signal-to-noise ratio is high enough this fitting technique can be used to derive the physical parameters that characterise the composite stellar-population: the *luminosity-weighted* age, metallicity and dust attenuation.

### 5.2.1 Distribution of the stellar populations

As shown in Appendix A, the results from simulations indicate that an individual spectrum does not have, in general, the required signal-to-noise ratio to derive accurate values of

the physical parameters that characterise the composite stellar population. However, the average spectra in concentric annuli do possess the required signal-to-noise, up to  $\sim 120$  arcsec ( $\sim 0.4\rho_{25}$  or  $\sim 5.4$  Kpc) in linear-projected galactocentric radii.

In order to study the distribution of the properties of the stellar population we obtained azimuthally averaged spectra by co-adding all the spectra in the mosaic within successive rings of 5 arcsec, starting from the central emission peak of the galaxy. These azimuthally averaged spectra were then analysed using the fitting procedure described above. Fig. 8 shows the radial distributions of the luminosity-weighted ages (left-panel) and metallicities (right-panel), derived by this method. The adopted error bars correspond to the typical errors estimated from the simulations (Appendix A) for a signal-to-noise ratio of  $\sim 100$ .

It is important to stress here that the accuracy of the absolute scale of the ages is not as good as the relative one, since the former is much more model dependent than the second. The age distribution shows, in general, a gradient, with older stellar populations at the central regions of the galaxy and younger ones at the outer regions. However, the oldest stellar populations are not found in the centre of the galaxy, but in a circumnuclear ring at  $\sim 25$  arcsec radius, with an inversion of the gradient at smaller radii. This region corresponds to the central kpc of the galaxy. At larger radii, the stellar population becomes steadily younger, at a rate of  $\sim 0.20$  Gyr/kpc, up to a radius of  $\sim 100$  arcsec ( $\sim 4.5$  kpc), and then becomes stable with an age of  $\sim 1$  Gyr, on average. On the other hand, the radial distribution of the metallicity of the stellar populations does not show such a clear trend, remaining nearly constant at any radii with a larger dispersion in the values. Both distributions show a similar shape than the one presented by (MacArthur et al. 2009), using a similar technique over classical slit-spectroscopy data, although their data show a larger dispersion.

The luminosity-weighted age and metallicity, derived from the plotted values are  $\sim 8.2$  Gyrs and  $Z \sim 0.01$  ( $[Z/H] \sim -0.27$ ), consistent with the values derived from the integrated spectrum Table 2.

The gradient found in the stellar population of NGC 628

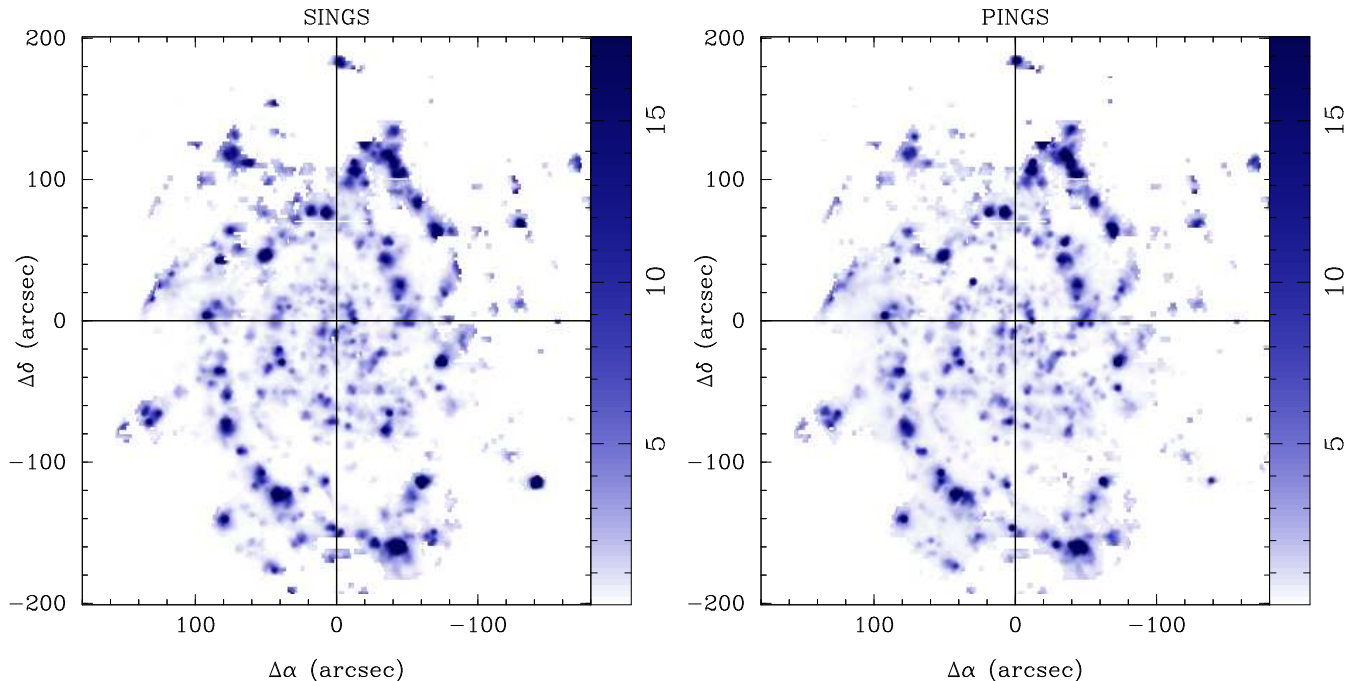


**Figure 9.** Left-panel: Reconstructed, continuum subtracted  $H\alpha$  narrow-band image of NGC 628 obtained after interpolating the aperture photometry extraction of the SINGS narrow-band image at the location of the mosaic fibres as in Fig. 4. Right-panel: Pure  $H\alpha$  emission lines map of NGC 628 calculated from the IFS mosaic in units of  $10^{-16} \text{ erg s}^{-1} \text{ cm}^{-2} \text{ arcsec}^{-2}$ . No correction for dust extinction was applied to the map. All morphological structures of the galaxy are completely reproduced in the IFS image.

(with the older stellar populations in the center), is common in late-type galaxies. Gadotti & dos Anjos (2001) found that  $\sim 60\%$  of this kind of galaxies show a negative color gradient in the  $U - B$  and  $B - V$  colors that it is most likely due to a gradient in the age of the stellar populations, with the younger populations in the outer regions. Differences between the colors in the central bulges (redder) and the outer disks (bluer) are also reported in other studies (e.g. Peletier & Balcells 1996). NGC 628 was included in the sample studied by Gadotti & dos Anjos (2001), and they reported a negative color gradient in this galaxy up to a radius of  $\sim 5$  arcmin, qualitatively in agreement with the trend found here based on the analysis of our IFS dataset.

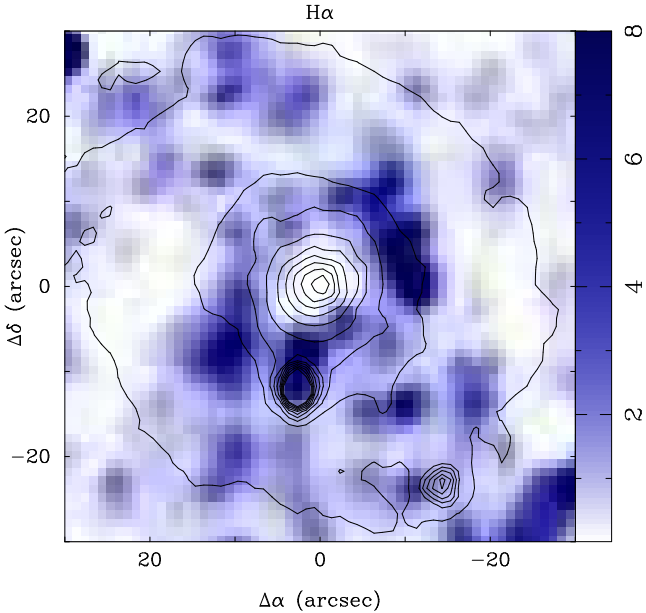
As mentioned before, Ganda et al. (2007) presented a study based on the IFS observation of the central core of NGC 628, using SAURON. The total field of view of their observation was  $33'' \times 41''$ , with a spatial sampling of  $\sim 1$  arcsec. This FOV fits inside one of our single pointings, being  $\sim 30$  times smaller in area than the FOV of the full dataset presented in this article. Due to the dithering technique applied at the central pointings, our final spatial resolution is just 2 times worse than their study. On the other hand, their spectral resolution is 2 times better than ours, with the penalty that their spectral coverage ( $4800 - 5300 \text{ \AA}$ ) is  $\sim 7$  times shorter than ours. Despite these differences, their results can be compared with the ones presented here for the inner regions.

Fig. 6 of Ganda et al. (2007) shows, among other things, the spatial distribution of the age and metallicity of NGC 628 derived from their analysis. Despite the very small FOV of their observations and the more reduced wavelength range sampled by their data, the basic structure described above can be seen. In particular, the age distribution ap-

pears flat in the inner 15 arcsec radius, with a ring of older stellar populations at  $\sim 20$  arcsec. On the other hand, the structure in the metallicity shown by Ganda et al. (2007) is more clumpy. The azimuthally averaged radial profile of both quantities, as presented in Fig A1a of that article, shows a clearer picture, with a similar trend in both parameters as shown in Fig. 8 for the same radii (although with an offset of the absolute values). The decline in the age of the stellar population inferred from our data at larger radii is out of the FOV of the SAURON observation.

Despite this qualitative agreement between both results, there are significant differences in the quantitative parameters. The values of age and metallicity derived by Ganda et al. (2007) for the central regions are younger ( $\sim 2$  Gyrs), and richer ( $Z \sim 0.0-0.2$ ), than the ones found by our analysis. These differences are due to the different technique used in both analysis. The analysis performed by Ganda et al. (2007) that we are comparing with, is based on a single stellar population fitting technique. Indeed, when we perform a similar analysis, adopting our fitting technique to compare with SSP, instead of allowing to mix multiple ones, we derive an age of  $\sim 1.4$  Gyrs, in a better agreement with the reported value.

As noted by the authors, the SSP analysis does not reflect perfectly well the complex starformation history of late-type galaxies. In particular, when a galaxy has undergone two separate bursts of star formation, the age derived by this analysis will be biased towards the one of the youngest stars, while the metallicity will be biased towards the one of the older population, as studied and described in detail by Serra & Trager (2007). Due to this effect, the authors refined their analysis of the stellar populations, constraining the metallicity by adopting the empirical relation between this



**Figure 10.** Zoom of the central  $\pm 30''$  region of the pure  $H\alpha$  emission lines map of NGC 628 calculated from the IFS shown in previous figure. The contour plots shows the continuum emission in the same region. The ionized ring described by Wakker & Adler (1995), and confirmed by Ganda et al. (2006) and Fathi07, is clearly seen.

value and the velocity dispersion, derived by Thomas et al. (2005). By adopting this constrain, they derive an age of 7.943 Gyrs and a metallicity of  $[Z/H] = -0.498$  for the stellar population of the NGC628 (Table 5 of Ganda et al. 2007), in a complete agreement with our results, listed in Table 2.

### 5.2.2 Distribution of the emission lines

The ionized gas in any spiral galaxy exhibits a complex structure, morphologically associated with the star-forming regions located along the spiral arms. To study their properties, these regions have perviously been targeted by narrow-band (e.g. Kennicutt & Hodge 1980) and Fabry-Perot imaging (e.g., Fathi07). In many cases these narrow-band images catch more than one single line (e.g.  $H\alpha$ , the  $[N II] \lambda\lambda 6548, 6584$  doublet or the  $[S II] \lambda\lambda 6716, 6731$  doublet), reducing their potential for the study the basic parameters of the ionized gas, or requiring certain assumptions about the actual line ratios included within the filter width (Kennicutt et al. 2008). IFS allows a much more refined decoupling of the different lines, and the production of maps of each individual emission line.

As in the case of the integrated spectra, in order to extract any physical information from the data set, we need first to identify the detected emission lines of the ionized gas and to decouple their emission from the stellar continuum. We use for this purpose the *clean* IFS mosaic version of NGC 628 (introduced previously in Section 5.1), which is free of bad fibres, foreground objects, and includes only those regions with high-quality spectrophotometric calibration, and fibres with an average flux along the whole spectral range greater than  $10^{-16} \text{ erg s}^{-1} \text{ cm}^{-2} \text{ \AA}^{-1}$ .

After this (relatively conservative) flux threshold was

**Table 6.** Number of fibres in different mosaic versions, the number in the *observed* mosaic refers to the total number of spectra considering all the pointings of NGC 628. The *clean* mosaic number corresponds to the remaining fibres after the flux threshold cut as explained in the text. The percentage stands for number of *clean* fibres with respect to the original mosaic.

Observed mosaic	Clean mosaic	Percentage
11094	6949	63%

applied, the number of fibres remaining in the *clean* mosaic was somewhat reduced, as shown in Table 6. The final number of spectra in the *clean* mosaic accounts for  $\sim 63\%$  of the total number of fibres in the original mosaic. The SSP fitting method was then applied to each individual spectrum of the clean mosaic, obtaining a residual spectrum per each fibre, in which the intensities for each detected emission line were measured following the techniques described in detail in Section 5. The statistical uncertainty in the measurement of the line flux was calculated by propagating the error associated to the multi-component fitting and considering the signal-to-noise of the spectral region.

As a result of the process described above, a set of measured emission line intensities (plus associated errors) was obtained for each observed spectrum of the final clean mosaic of NGC 628. From these sets of emission line intensities, emission line maps were created by interpolating the intensities derived for each individual line in each individual spectrum, based on the position tables of the clean mosaics, and correcting for the dithering overlapping effects when appropriated. The interpolation was performed using E3D, adopting a natural-neighbour, non-linear interpolation scheme, with a final scale of  $1''/\text{pixel}$  in the resulting maps. Regions in the borders of the mosaics and/or large regions in between the mosaic without signal are prone to artifacts created by the interpolation scheme, special masks were created in order to deal with those regions. Further, as many of the derived maps are based on a reliable measurement of  $H\beta$ , a flux threshold mask was created for each mosaic for those regions with an integrated  $H\beta$  flux per fibre below  $10^{-16} \text{ erg s}^{-1} \text{ cm}^{-2}$  (i.e.  $0.2 \times 10^{-16} \text{ erg s}^{-1} \text{ cm}^{-2}$  per pixel), which corresponds to a detection limit of  $\sim 5\sigma$ . This conservative limit has been adopted to avoid contaminating our results with low signal-to-noise data, and to grant the accuracy of the absolute spectrophotometry.

Practically any emission line map (or a combination of them) can be constructed from the detected emission lines in the mosaic. In this section, we present a number of maps corresponding to the most important emission lines and derived quantities of interest<sup>6</sup>. The right-panel of Fig. 9 shows the pure  $H\alpha$  emission line intensity map in units of  $10^{-16} \text{ erg s}^{-1} \text{ cm}^{-2} \text{ arcsec}^{-2}$ , obtained by the procedure described previously. For a purely qualitative comparison purpose, the left-panel of the same figure shows the continuum-subtracted  $H\alpha$  narrow-band image of NGC 628 extracted from the SINGS ancillary data by interpolating the aperture photometry extraction at the location of the mosaic fibres as described in Section 4.1. A visual inspec-

<sup>6</sup> accesible at <http://www.ast.cam.ac.uk/research/pings/html/public/>

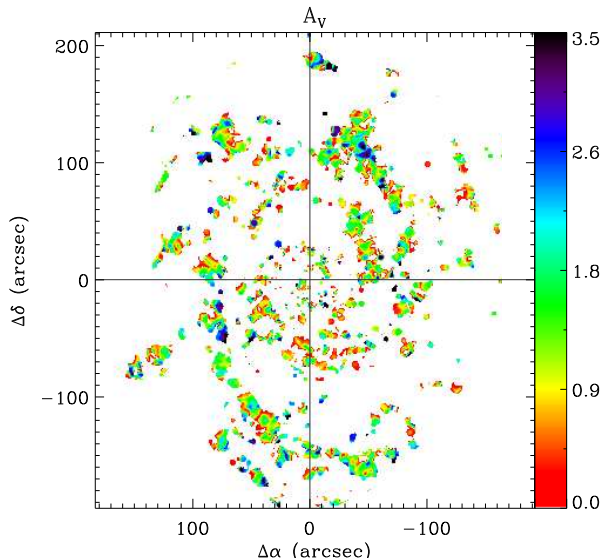


**Figure 11.** Dust attenuation map of the ionized gas ( $A_V$ ), derived by comparing the measured  $H\alpha/H\beta$  line ratio map with the expected value for case-B recombination, assuming a homogeneous distribution of the electron density and temperature, and the attenuation law by Cardelli et al. (1989). The regions without accurate measurements of either emission lines were masked.

tion of both maps shows that they match remarkably well in terms of the morphology. As the dominant gas ionization mechanism giving rise to the emission line in this galaxy is due to hot (OB) stars (Section 5.1.2), the  $H\alpha$  line intensity map shown in Fig. 9 traces the star-forming regions in this galaxy. The map displays a distinctive spiral structure with multiple H II regions and H II complexes of different sizes and morphology along the spiral arms. The brightest sources are located at the outer regions of the galaxy, with a particular giant region located at  $(\Delta\alpha, \Delta\delta) \sim (-40, 120)$  arcsec. From this map we can also note the presence of diffuse emission along the spiral arms and in the intra-arms regions.

Fathi07 has recently provided with a similar  $H\alpha$  map, with twice the field-of-view of our IFS data, on the basis of Fabry-Perot and complementary narrow-band images. The distribution shown by both maps are remarkable similar. They identified 376 H II regions, many of them within the field of view of our IFS data. A detail comparison of each of these individual sources, and an analysis of their spectroscopic properties will be presented elsewhere (Rosales-Ortega in prep.).

Their data confirm the presence of a central structure in NGC 628, characterized by a ring of ionized gas at  $\sim 15\text{--}20''$ , already described by Wakker & Adler (1995) and Ganda et al. (2006) in their  $H\beta$  and [O III] emission line distributions. Figure 10 shows a zoom of the  $H\alpha$  distribution already shown in Figure 9 (right panel), together with a counterplot of the continuum emission in the V-band (fig. 4, right panel). The spatial resolution for this region is better than the one in the overall Mosaic, due to the dithering performed only in the central pointing. The slightly oval ring structure in the ionized gas is clearly identified in the  $H\alpha$  map, showing a remarkable similarity with the  $H\beta$  distribution shown by Ganda et al. (2006). It is interesting to note

here that despite the difference in the original sampling of the SAURON instrument (used by Ganda et al. 2006, 2007), and PPAK, the apparent resolution of both maps are very similar. This ring is detected, at different levels, in all of the emission line splices analyzed in the current article, following the same basic morphological pattern.

### 5.2.3 Distribution of the dust attenuation

Besides the intrinsic significance of the emission lines map presented previously, the most interesting application of the 2D distribution of the different line intensities resides in the calculation of well-known line ratios that can be translated to physical properties of the emitting gas. With the aid of the IFS data we can investigate for the first time, the point-to-point variation of these physical properties over a considerable area on the surface of a galaxy.

Fig. 11 shows the distribution of the dust extinction derived from the  $H\alpha/H\beta$  line ratio, in terms of the visual extinction  $A_V$  (in magnitudes), assuming, as in the case of the analysis of the integrated spectrum, case-B recombination with an electron temperature of  $T_e \sim 10^4$  K, and adopting the Cardelli et al. (1989) extinction law with  $R_V$ , the total to selective extinction ratio, equal to 3.1. Although other Balmer lines were detected at different locations in the galaxy,  $H\alpha$  and  $H\beta$  are obviously the lines with the highest signal-to-noise and therefore are the most adequate for the determination of  $A_V$ . The dust extinction map was derived for those locations where the intensity of the  $H\beta$  line was above the adopted flux threshold. These regions clearly follow the spiral arm structure. The dust shows a clumpy distribution, a rich structure and large variations even within the same H II region or complex. There is no apparent trend of the extinction along the spiral arms or in any radial direction. The average extinction derived from the values shown in the map is  $A_V \sim 1.24 \pm 0.76$  mag, which is slightly larger but comparable to the value derived using the integrated spectrum ( $A_V \sim 1.04$ ). The reason for this discrepancy may reside in the fact that the ionized gas component of the integrated spectrum is dominated by the spectra of the outer regions, where the intensity of the emission lines is stronger and the extinction is somewhat lower. Extinctions greater than 2.5 are found in specific regions, e.g. the central zone of the giant H II complex at  $\sim (-40, 120)$ , while others are found in compact H II regions along both spiral arms. Previous studies have estimated the extinction at different locations within this galaxy targeting individual H II regions (e.g. McCall et al. 1985; Belley & Roy 1992; Petersen & Gammelgaard 1996), the derived extinctions from these studies are consistent with the range of  $A_V$  values found in this work.

### 5.2.4 Ionization conditions

As discussed previously in Section 5.1.2, the source and structure of the ionization can be in principle investigated by exploring the line ratio maps of typical diagnostic indices. Fig. 12 shows on the left-panel the line ratio map of [N II]  $\lambda 6584/H\alpha$  ( $N_2H\alpha$ ) and on the right-panel, the [O III]  $\lambda 5007/H\beta$  ( $O_3H\beta$ ) ratio map, in logarithmic scale. Note that, given the proximity of the emission lines, these

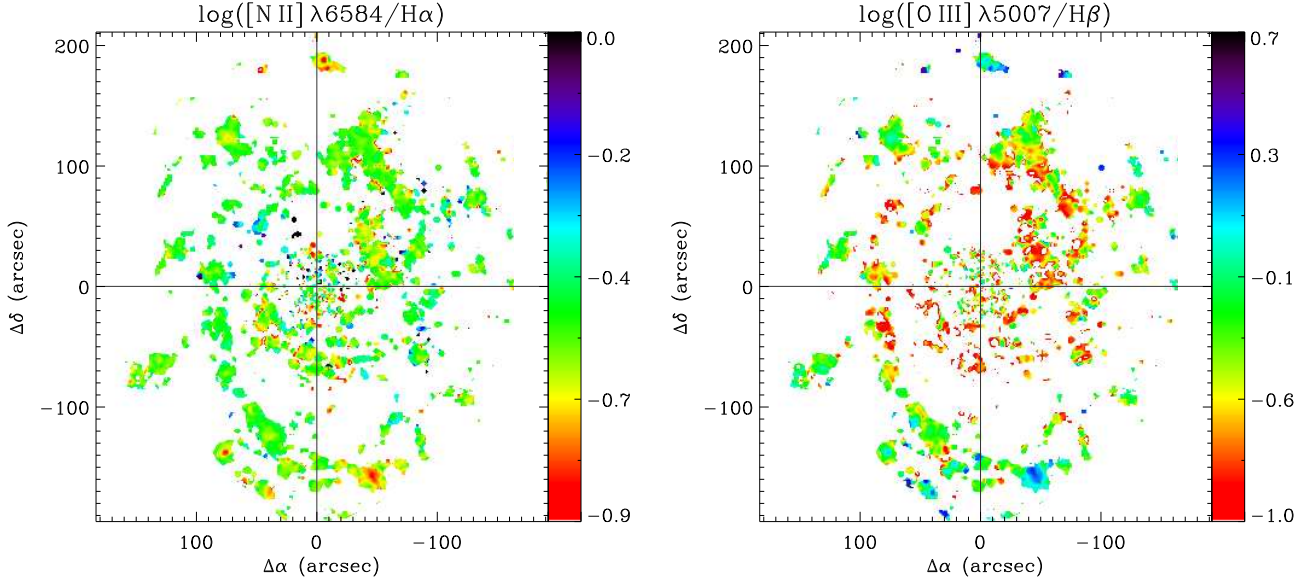


**Figure 12.** 2D spatial properties of NGC 628, classical diagnostic line ratio maps. Left-panel:  $[\text{N II}] \lambda 6584/\text{H}\alpha$  line ratio map. Right panel:  $[\text{O III}] \lambda 5007/\text{H}\beta$  line ratio map; both in logarithmic scale.

indices are almost reddening-independent. The  $N_2H_\alpha$  shows a very homogeneous behaviour, with small variations in individual regions, some of them showing lower values in the central part of the regions (e.g the knot at  $\Delta\alpha, \Delta\delta \sim 40, -130$ ). The average ratio derived from this map is  $-0.55 \pm 0.12$  dex, which is excellent agreement with the value derived from the integrated spectrum ( $N_2H_\alpha = -0.56$ ). However, some regions at the outer part of the galaxy show lower ratios consistent with values  $\sim -0.75$ , e.g  $(\Delta\alpha, \Delta\delta) \sim (-50, -160)$ ,  $(0, 200)$ ,  $(-100, 100)$ , which might suggest a gradient of this index decreasing from the inner to the outer regions of the galaxy. On the other hand, the  $O_3H_\beta$  shows a clear gradient along the spiral arms with lower ratios towards the inner regions and greater values at the outer part of the galaxy. The average value of this index derived from the map is  $-0.50 \pm 0.25$  dex, which again is in good agreement with the integrated value of  $-0.48$ . It is interesting to note that the regions with the highest values of  $O_3H_\beta$  are coincident with the zones of the lowest  $N_2H_\alpha$  ratios. Given that the  $[\text{N II}]$  emission originates in the singly ionized regions, between the fully ionized and the partially ionized zones, the  $N_2H_\alpha$  ratio traces the changes in the local ionization, while the  $[\text{O III}]$  originates in the fully ionized zones, tracing the strength of the ionization. Therefore, the distribution found in these diagnostic maps may indicate that the ionization is stronger in the outer parts of the spiral arms, than in the central regions. The values of both ratios at any location in the galaxy are consistent with ionization produced by hot OB stars, as expected. In particular, there is no evidence of ionization due to shocks and/or nuclear activity.

An additional way of studying the 2D distribution of the galaxy properties consist in obtaining azimuthally-averaged radial spectra, from which radial average properties can be derived. Taking again as a base the *clean* IFS mosaic version of the galaxy, radial average spectra were obtained by co-adding all the spectra within successive rings of 10 arcsec, starting from the central reference point. An average

spectrum was obtained for each single annulus at a given radius. The radial average spectra were then analysed using the same fitting procedures described before. Although the derived spectra present more signal-to-noise than the single-fibre case, the measured emission lines were corrected by extinction using only the  $\text{H}\alpha/\text{H}\beta$  ratio for consistency with the previous method.

Fig. 13 shows the BPT diagnostic diagram (Baldwin et al. 1981) for the  $N_2H_\alpha$  and  $O_3H_\beta$  line ratios. The bluish-asterisk symbols (in the online version) correspond to the derived values of the emission line ratios for 300 randomly selected spectra distributed uniformly over the surface covered by the emission line ratio maps shown in Fig. 12. The reddish diamonds correspond to the radial average values introduced above, while the red solid-square indicates the average line ratio derived from the integrated spectrum of the galaxy. The colour-coding of both the individual fibres and the radial-average samples is related to the spatial position of a given fibre/annulus. Lighter tones correspond to the inner regions of the galaxy, while darker colours correspond to positions with increasing galactocentric radius (arrow direction). The dark-thick line corresponds to the theoretical boundaries dividing the starburst region from other types of ionization using the parametrization provided by Kewley et al. (2001). The dashed lines represent the  $\pm 0.1$  dex variation. As expected, the ionization is dominated by hot stars (OB class) associated with star-forming regions, at any location in the galaxy. A clear trend can be noticed in Fig. 13 for both samples, the spectra corresponding to the inner regions tend to have lower line ratios for both indices; for regions at the outer part of the galaxy, the ratios increase approaching the theoretical boundary. Part of the reason for this behaviour is that inner parts of the galaxy lack emission in  $[\text{O II}]$  and  $[\text{O III}]$ , while towards the outer parts, the emission from these species is prominent, increasing the two line ratios involved in this diagram

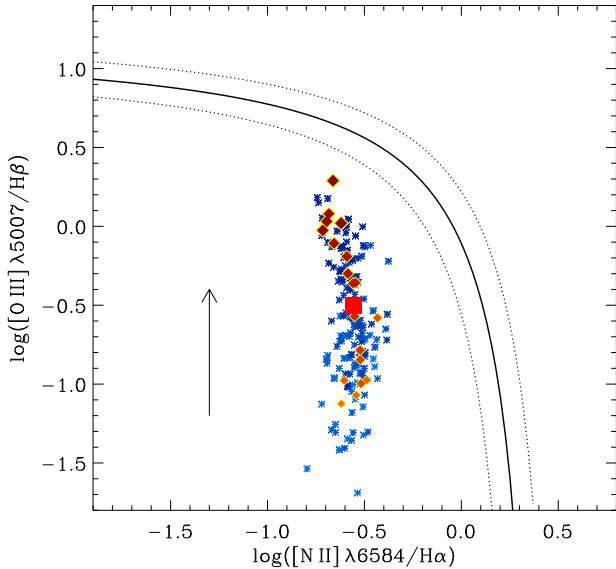


**Figure 13.**  $N_2H_\alpha$  vs.  $O_3H_\beta$  diagnostic diagram for NGC 628. The bluish symbols correspond to the derived values of the emission line ratios for 300 randomly selected spectra distributed uniformly over the surface covered by the emission line ratio maps shown in Fig. 12. The reddish diamonds correspond to the azimuthally-averaged radial values. The red solid-square indicates the ratio derived from the integrated spectrum of the galaxy. Lighter tones correspond to inner regions of the galaxy, darker colours to increasing galactocentric distance, outlined by the arrow. In the radial case, the size of the symbols increases with radius.

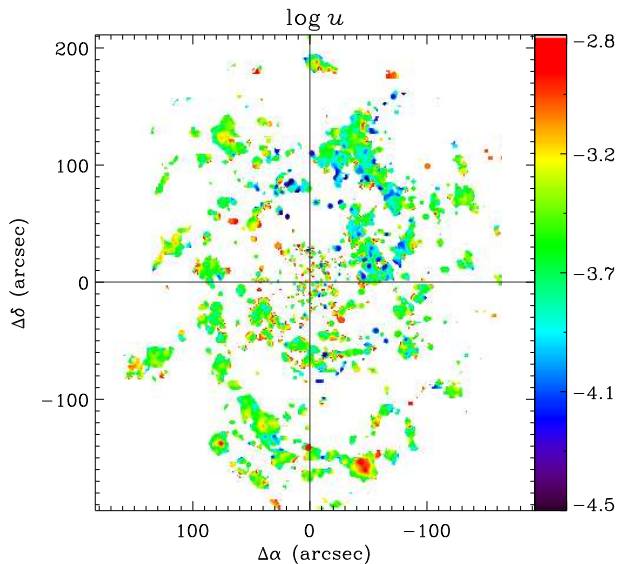


**Figure 14.** Distribution of the ionization parameter  $\log u$ , in logarithmic scale, derived from the dust corrected  $[O II] \lambda 3727/[O III] \lambda 5007$  line ratio.

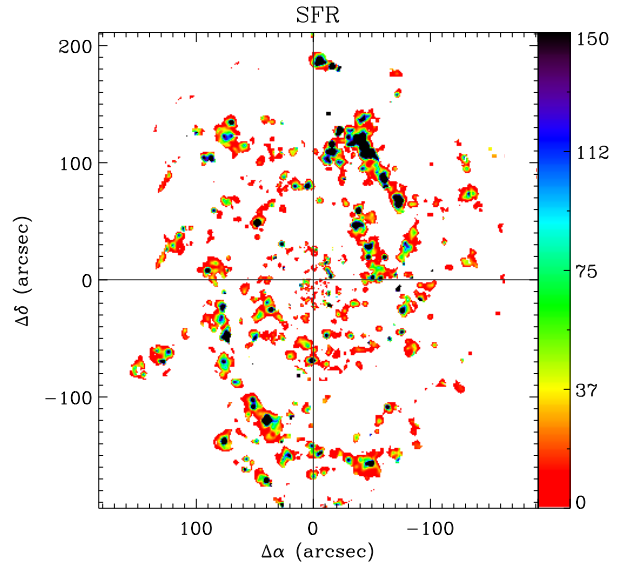


**Figure 15.** Surface star-formation rate (SFR) in units of  $10^{-5} M_\odot \text{ yr}^{-1}$ , derived from the  $H\alpha$  line intensity map shown in Fig. 10, after correcting by dust attenuation. This map traces the distribution of the ionized gas, not the young stars, which form much more compact structures than the ones shown in the figure.

The differences in the line ratios at different locations in the galaxy may be also driven by the strength of the ionization field, being stronger in the regions with higher  $N_2H_\alpha$  line ratio, and lower  $O_3H_\beta$  one. In order to investigate this point, Fig. 14 shows the distribution of the ionization parameter in logarithmic scale,  $\log u$ , calculated accordingly to Equation 1 (Díaz & Pérez-Montero 2000), which is based on the dust-corrected  $[O II]/[O III]$  ratio. Both lines were corrected by extinction using the  $A_V$  map discussed previously. The  $\log u$  map shows that the ionization is indeed stronger in the outer parts of the spiral arms, as the previous maps suggested. However, we can also distinguish a good degree of ionization structure in individual regions within the spiral arms, with higher values of  $\log u$  corresponding to the geometrical centroids of the H II regions, as one might expect in the scenario of a central star cluster or association embedded within an H II region. Given that the dominant source of the ionization is radiation from OB stars, this result indicates that the star-formation rate is stronger in the outer regions of the galaxy. A striking feature of this map is the presence of regions with low values of the ionization parameter (blue colour) located mainly in a specific region, corresponding to the first quadrant, north-west part of the galaxy. These low  $\log u$  regions are found mainly at the edges of giant H II complexes, but they are also found as individual regions. The nature of these low ionization regions will be investigated thereafter. The mean value of  $\log u$  derived from this map is  $-3.50 \pm 0.26$  dex, which is 0.08 dex higher than the value derived from the integrated spectrum of NGC 628.

### 5.2.5 Surface star-formation rate

The surface SFR can be derived using the emission line distribution of  $H\alpha$  or  $[O II] \lambda 3727$ . However, the latter line

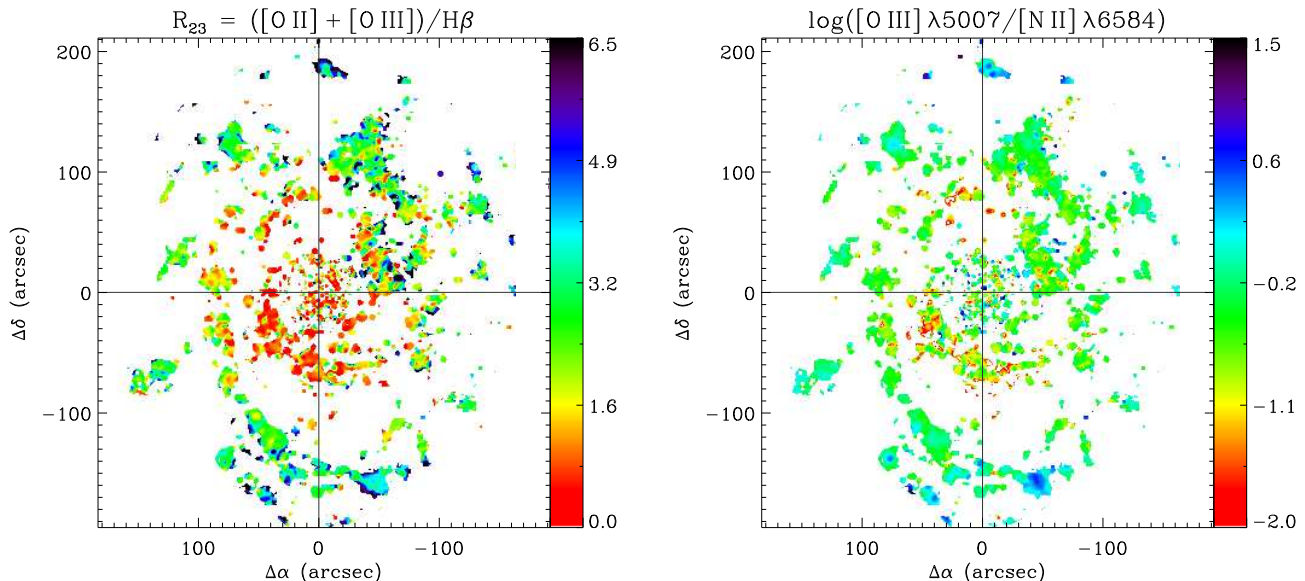


**Figure 16.** 2D distribution of the  $R_{23}$  and  $[\text{O III}]/[\text{N II}]$  metallicity indices for NGC 628. Both maps show a gradient of lower values in the inner regions to higher values to the outer part of the galaxy.

suffers from more inaccuracies in both the spectrophotometric calibration and flux determination, since it lies just at the blue edge of the spectral range covered by our data set. Therefore, only the  $\text{H}\alpha$  intensity map was used in this analysis. Following our previous prescription to derive the integrated SFR of the galaxy, the  $\text{H}\alpha$  intensity map was corrected for attenuation, adopting the dust distribution described in Section 5.2.3, and the same attenuation law as in Section 5.1. Then, the dust corrected flux densities were transformed to absolute luminosities, using the same distance and cosmology described before. These luminosities were used to obtain the surface SFR, by adopting the classical relations described by Kennicutt (1998).

Fig. 15 shows the derived distribution for the surface SFR, in units of  $10^{-5} M_{\odot} \text{ yr}^{-1} \text{ arcsec}^{-2}$ . As expected, the stronger star-formation is distributed in clumps along the spiral arms, following a similar morphology to the distribution of the  $\text{H}\alpha$  emission (i.e. the H II regions). In addition, the direct transformation between extinction corrected  $\text{H}\alpha$  flux and SFR produce an apparent, low level, star-formation rate in the inter-arms regions, two orders of magnitude lower than that of the H II regions. However, it is unclear how closely is associated this derived SFR with the inter-arm  $\text{H}\alpha$  emission. Ionizing photons leaking from the H II regions and stochasticity in the conversion between both parameters may become important at this intensity level. As already shown by the distribution of the  $N_2\text{H}\alpha$  and  $\text{O}_3\text{H}\beta$  line ratios (Fig. 12), and the ionization parameter (Fig. 14), there is an increase of the star-formation rate from the inner to the outer regions of the spiral arms.

The global SFR can be derived by co-adding the surface SFR over the area shown in the figure, obtaining a value of  $\sim 1.1 M_{\odot} \text{ yr}^{-1}$ . By applying the same aperture and sampling correction applied to the integrated  $\text{H}\alpha$  flux in Section 5.1, the estimated SFR is  $\sim 2.4 M_{\odot} \text{ yr}^{-1}$ , which is practically identical to the estimate derived based on the flux of  $\text{H}\alpha$  in the integrated spectrum.

#### 5.2.6 Distribution of the gas-phase oxygen abundance

One of the main purposes of the PINGS dataset is to study the metallicity content of the galaxy in a 2D context. As discussed previously, the oxygen abundance is normally derived using a variety of diagnostic methods based on strong lines, from which the most common one is the  $R_{23}$  indicator. The dust-corrected emission line maps of  $[\text{O II}]$  and  $[\text{O III}]$  provide the means to explore the behavior of this indicator. The left panel of Fig. 16 shows the  $R_{23}$  map of NGC 628. From a first visual inspection, it is evident that the map presents a clear gradient of lower values of  $R_{23}$  in the inner regions of the galaxy, to higher values to the outer parts, specially along the spiral arms. The average  $R_{23}$  value derived from the map is  $2.41 \pm 1.37$ , which is in good agreement with the value inferred from the integrated spectrum ( $R_{23} = 2.57$ ). The lower values of  $R_{23}$  in the central regions of the galaxy are expected, given the low emission of  $[\text{O II}]$  and (especially)  $[\text{O III}]$ , as inferred in figure Fig. 13. For well-defined H II regions, the value of  $R_{23}$  seems to be constant in the majority of the cases; however, there are regions in which the value of  $R_{23}$  varies within the H II region or complex, showing some level of structure. Considering the O/H values derived after different calibrators from the integrated spectrum of NGC 628 in Section 5.1.3 ( $12 + \log(\text{O}/\text{H}) \sim 8.7$ ), and previous abundance determinations from individual H II regions in this galaxy (e.g. McCall et al. 1985; Ferguson et al. 1998), suggest that the average oxygen abundance of NGC 628 corresponds to the high metallicity regime. In this scenario, the double-valued nature of the  $R_{23}$  index can be broken, and the gradient of higher-to-lower values of  $R_{23}$  from the inner to the outer parts of the galaxy shown in this map would correspond to the decrement of the  $R_{23}$  ratio in the upper-branch of a O/H vs.  $R_{23}$  diagram, and therefore, to a true metallicity gradient of the galaxy, as previous studies based on individual H II regions have shown.

Another popular metallicity-sensitive index is given by

the [O III]  $\lambda 5007$ /[N II]  $\lambda 6584$  ratio. Pettini & Pagel (2004) suggested the use of this ratio (in a modified version) as abundance indicator suitable for the analysis of high-redshift galaxies. However, the direct application of this indicator may be too simplistic, the reasons being that the [O III]/[N II] ratio is strongly dependent on the excitation of the nebula, and it is also sensitive to both the ionization parameter and to the age of the cluster of exciting stars (Dopita et al. 2000). As suggested by Dopita et al. (2006), the [O III]  $\lambda 5007$ /[N II]  $\lambda 6584$  ratio can only be used as an abundance indicator only when a characteristic age of the exciting clusters can be assumed, and its application in single galaxies should be taken with caution. However, the combination of this ratio with, for example, the [N II]  $\lambda 6584$ /[O II]  $\lambda 3727$  ratio, can provide a good diagnostic of both metallicity and age of the ionizing source (Dopita et al. 2006). The right panel of Fig. 16 shows the map of the [O III]  $\lambda 5007$ /[N II]  $\lambda 6584$  ratio of NGC 628 in logarithmic scale. It is worthy to note that this ratio spans for more than two orders of magnitude. Similarly to the  $R_{23}$  map, this panel shows a gradient of lower values of the [O III]/[N II] ratio from the inner part of the galaxy, to higher values in the outer parts. The average value derived from the map is  $-0.35 \pm 0.36$  dex, compared to  $-0.40$  obtained from the integrated spectrum. The map shows a smoother distribution within individual regions compared to the  $R_{23}$  map. With the corresponding cautions considering the known dependences of this index with the functional parameters of the H II regions, the [O III]/[N II] gradient found for NGC 628 would correspond to a metallicity gradient of the galaxy, with some level of inhomogeneity in individual regions as shown in this map. In order to determine the existence of abundance variations within the same region of the galaxy, it would be required to co-add the spectra corresponding to regions with similar ionization conditions, and then perform an analysis based on single regions. This detailed analysis, together with a complete study of the radial abundance gradient of this galaxy will be presented in a forthcoming paper (Rosales-Ortega et al. in preparation).

In Fig. 17 we present the oxygen abundance 2D map of NGC 628 based on the O3N2 calibrator in units of  $12 + \log(\text{O}/\text{H})$ , obtained by the manipulation of the emission line maps presented before. No other 2D abundance maps were attempted since the parametrizations of the different calibrators do not allow a simple image manipulation (large blank areas produce convergence problems which limits the application of any interpolation routine). However, as discussed previously in Section 5.1.3, the O3N2 abundance determination follows qualitatively the same pattern as the other more elaborated calibrators based on  $R_{23}$  and the  $\text{ff}-T_e$  relation. The map of Fig. 17 shows a clear gradient of higher oxygen metallicity values from the inner part to the outer part of the galaxy, and along the spiral arms. The most metal deficient regions are found at the extremes of the spiral arms, a prominent region is found at  $(\Delta\alpha, \Delta\delta) \sim (-40, -60)$ . The average value of the oxygen abundance derived from this map is  $8.75 \pm 0.17$ , which is equivalent to the oxygen abundance derived from the integrated spectrum using the same calibrator, i.e.  $8.71 \pm 0.11$ .

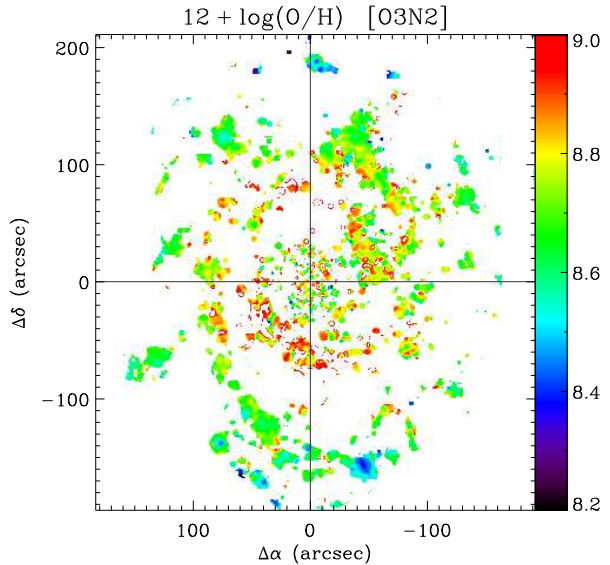


**Figure 17.** Oxygen abundance map of NGC 628 derived by applying the O3N2 calibrator (Pettini & Pagel 2004) to the emission line maps of the galaxy. The figure shows a clear gradient in metallicity, with more abundant regions in the inner part of the galaxy.

**Table 7.** Summary of the main properties of the galaxy.

Parameter	Integrated	Average
Age (Gyr)	8.95	
[Z/H]	-0.44	
$A_V$ stellar (mag)	0.4	
$A_V$ (mag)	1.04	$1.24 \pm 0.76$
$\log([\text{N II}] \lambda 6584/\text{H}\alpha)$	-0.56	$-0.55 \pm 0.12$
$\log([\text{O III}] \lambda 5007/\text{H}\beta)$	-0.48	$-0.50 \pm 0.25$
$\log u$	-3.58	$-3.50 \pm 0.26$
SFR ( $M_\odot \text{ yr}^{-1}$ )	2.4	2.4*
$\log R_{23}$	0.41	$0.38 \pm 0.13$
$\log([\text{O III}] \lambda 5007/[\text{N II}] \lambda 6584)$	-0.40	$-0.35 \pm 0.36$
$12 + \log(\text{O}/\text{H})_{\text{O3N2}}$	$8.71 \pm 0.11$	$8.75 \pm 0.17$
$12 + \log(\text{O}/\text{H})^\dagger$	$8.69 \pm 0.31$	

\* Co-added.

† Mean abundance among the various empirical calibrators.

## 6 DISCUSSION AND CONCLUSIONS

In this article we presented wide-field IFS observations of a substantial fraction of the nearby galaxy NGC 628 ( $\sim 70\%$  of its projected optical size). The observations were performed by adopting a mosaicking procedure, using the PPAK IFU (mounted at the 3.5m telescope at Calar Alto), which provides a sampling of 2.7 arcsec and a FOV larger than 1 arcmin (diameter). The total dataset comprises 11094 individual spectra, covering a nearly circular FOV of  $\sim 6$  arcmin in diameter, centered on the bulge of the galaxy. To our knowledge, this is the largest spectroscopic survey ever made of a single nearby galaxy. A detailed flux calibration technique has been applied, which granted a spectrophotometric accuracy of  $\sim 0.2$  mag, down to a surface brightness of  $\sim 22$  mag arcsec $^{-2}$ , comprising 6949 spectra from the original dataset.

The spectrophotometrically calibrated data have been analysed both as a single integrated spectrum, which characterises the global properties of the galaxy, and using each individual spectrum to determine the spatial variation of galaxy properties. The stellar and ionized gas components have been decoupled by a fitting technique which uses SSP templates and single Gaussian functions respectively to characterise these components. The main properties extracted from the analysis of the stellar continuum emission were the *luminosity-weighted* ages, metallicities and dust attenuation of the composite stellar population. On the other hand, for the gas content, we derived the morphology of the ionized gas, the dust content, the spatially resolved SFR, the source of the ionization, and the oxygen abundance.

Table 7 lists the main properties derived in this study for NGC 628. For each of the estimated parameters we list the values derived based on the analysis of the integrated spectrum (labelled as Integrated), and the average values derived from the 2D maps (labelled as Average). When more than one technique was used to derive the values, we listed the values derived using the same technique for both datasets. In all cases, the derived values are compatible.

Regarding the spatial distribution of the different analysed properties, a gradient was found in the *luminosity-weighted* age of the stellar populations from the central regions, having older stellar populations, to the outer regions, having younger components. On the other hand, the radial dependence of the stellar metallicity is weaker, showing a slight or no gradient. If there is any gradient, the richer stellar populations are located at the central regions, while the poorer ones are at the outer regions. All together these results are consistent with our current understanding of how the late-type galaxies grow along cosmological epochs, that is inside-out (Barden et al. 2005). The older and more metal-rich stellar populations, formed before, on the basis of recycled gas from previous populations, are located in the center, while the younger and less metal rich stars are in the outer regions. It is interesting to note that the oxygen abundance in the ionized gas follows nearly the same distribution (Fig. 17), with larger abundances in the inner regions and lower abundances in the outer ones. This gradient was previously reported by McCall et al. (1985), and confirmed by Belley & Roy (1992), van Zee et al. (1998) and Ferguson et al. (1998).

In the case of the stellar populations, there seems to be an inversion of the age gradient at the very centre of the galaxy ( $\sim 1$  kpc), where apparently there exist a ring of old stars at this distance, with a trend to younger ones at the very center. These results were previously reported by Ganda et al. (2007), on the basis of their IFS observations at the very centre of this galaxy. Similar results have been reported in other galaxies, mostly Sa/S0, where the inner regions of their bulges present bluer colors, consistent with younger stellar populations (e.g. Deharveng et al. 1997). According to this scenario, the circumnuclear star-formation rings detected in Sa-Sbc galaxies might show evidence of gas transfer due to radial motions in these galaxies (e.g. Knapen et al. 2006).

Spatially-resolved maps of the emission line intensities and physical properties were derived for NGC 628. Contrary to previous attempts to perform a 2D wide-field analysis based on narrow-band (or Fabry-Perot) imaging, which only

allowed a basic analysis of the physical parameters and/or required assumptions on the line ratios included within individual filters (e.g. H $\alpha$ ), the emission line maps presented in this paper were constructed from individual (deblended) emission lines at any discrete spatial location of the galaxy, where enough signal-to-noise was found. This fact allowed to investigate the point-to-point variation of the physical properties over a considerable area on the galaxy. Extinction, ionization, and metallicity-sensitive indicators maps were derived from reddening corrected emission line maps. In general, they show that the ionized gas in these spiral galaxies exhibits a complex structure, morphologically associated with the star forming regions located along the spiral arms.

In general, it is found that the dominant ionization process is due to the OB hot-stars associated with star-forming regions, based on the distribution of the classical diagnostic lines. The ionization is stronger along the spiral arms, associated with the HII regions, and more intense in the outer than in the inner ones. Indeed, the surface SFR is an order of magnitude stronger in the outer HII regions, at distance larger than  $\sim 100$  arcsec (4.5 kpc), than in the inner ones. Considering that in these outer regions there is a lower mass density, the growing rate of stellar mass is considerably larger there than in the inner ones. Therefore, even taking into account the circumnuclear star-formation rate, the growth of the galaxy is dominated by the inside-out process.

There is growing evidence of a central structure in NGC 628, widely discussed by Fathi07. This structure is characterized by a ring of ionized gas (Wakker & Adler 1995; Ganda et al. 2006; Fathi et al. 2007), and a drop in the  $B-V$  colors (Natali et al. 1992; Fathi et al. 2007). The kinematics analysis of the stellar and gas component within this ring, in comparison with that of the rest of the galaxy, indicates that there is a rapidly rotating component, most probably a dynamically cold disc, which could be built by inflow from the outer parts towards the center (Daigle et al. 2006; Ganda et al. 2006; Fathi et al. 2007). Fathi07 found that this circumnuclear ring is that the expected location of the inner Lindblad resonance radius, where the gas is indeed expected to accumulate, due to non-circular motions exerted by a bar or spiral arms. This gas concentration may lead to a low luminosity starburst (e.g., Knapen et al. 1995). Our results show, for the first time, that (1) the gas in the circumnuclear ring is ionized by starformation, and (2) the ring is spatially coincident with a decrease in the luminosity-weighted ages of the stellar populations, which causes the previously observed drop in the  $B-V$  colors. All together, they support the interpretation outlined by Fathi07.

The integrated spectrum of the galaxy was used to analyse the chemical abundance of the galaxy by means of different empirical diagnostic abundance calibrators. We confirmed the validity of the determination of the integrated chemical composition of a galaxy through the analysis of the global-emission line spectra, as previously found by other authors (Kobulnicky et al. 1999; Pilyugin et al. 2004; Moustakas & Kennicutt 2006a), under the assumption that the observed emission lines arise via photoionization from young, massive stars. From the set of calibrators used for this purpose, the  $R_{23}$  methods based on photoionization modelling provide higher values of the oxygen abundance

(i.e. M91 & KK04), followed by those methods which consider one of two emission-line indices (N2, O3N2) and the  $f\text{-}T_e$  method. The differences between different calibrators are as large as  $\sim \pm 0.7$  dex, especially for the high values of O/H derived from the  $R_{23}$  methods compared to the other ones. If an arbitrary negative offset is applied (as suggested by the literature), the O/H values seem to be consistent for an average integrated oxygen abundance of NGC 628 of  $12 + \log(\text{O}/\text{H}) \sim 8.7$ , in agreement with previous studies. Note that the validity of the abundance determination depends mainly on the chosen calibrator used to derive the chemical composition, and to a second order, on the SSP fitting decoupling.

The spatially resolved distribution of the abundance shows a clear gradient of higher oxygen metallicity values from the inner part to the outer part of the galaxy, and along the spiral arms Fig. 17. However, in some instances, the value of the oxygen abundance (and other physical properties like extinction and the ionization parameter) varies within what would be considered a classical well-defined H II region (or H II complex), showing some level of structure. Indeed, the 2D character of the PINGS data allow us to study the small-scale variation of the spectra within a given emitting area. As suggested in Paper I, the values of the emission line ratios measured using different extraction apertures vary considerably as a function of the aperture size, and that the scatter of the central value is larger than the statistical error in the measurements, reflecting that this might in fact be a physical effect. If we take as a premise that for a sufficiently large H II region, the emission line measurements are aperture and spatial dependent, i.e. that the light is emitted under different physical conditions, by gas in different degrees of ionization, and modified by different amounts of reddening (and therefore providing different elemental ionic abundances), the level of structure seen in the 2D maps of NGC 628 may be due to the intrinsic distribution of the ionizing sources, gas content, dust extinction and ionization structure within a given region, i.e. we would be sampling real point-to-point variations of the physical properties within a H II region.

The emission line maps presented in this paper proved to be useful in describing the general 2D properties of the selected galaxies. However, the conclusions raised from them were based on general trends that depend, to a certain level, on the interpolation scheme applied in order to derive the pixel-resolved maps. More robust conclusions can only be drawn by analysing specific individual regions within the given galaxy, or by co-adding spectra of regions with the same physical properties and comparing the results in the 2D context. This approach will be followed in subsequent papers in order to study the spatially-resolved spectroscopic properties of this and the rest of the PINGS galaxies.

## ACKNOWLEDGMENTS

SFS thanks the Spanish Plan Nacional de Astronomía program AYA2005-09413-C02-02, of the Spanish Ministry of Education and Science and the Plan Andaluz de Investigación of Junta de Andalucía as research group FQM306, and the ARAID fundation for providing funds.

SFS thanks the director of CEFCA, Dr. M. Moles, for the unconditional support to this project.

FFRO would like to thank the Mexican National Council for Science and Technology (CONACyT) and the Dirección General de Relaciones Internacionales (SEP-Mxico). We would like to thank the referee, R. Peletier, for the very valuable comments and suggestions which improved the final content of this paper. We acknowledge Dr. N. Cardiel for his help in the study of the stellar populations.

## REFERENCES

- Aaronson M., Cohen J. G., Mould J., Malkan M., 1978, *ApJ*, 223, 824
- Alloin D., Collin-Souffrin S., Joly M., Vigroux L., 1979, *A&A*, 78, 200
- Bacon R., Copin Y., Monnet G., Miller B. W., Allington-Smith J. R., Bureau M., Carollo C. M., Davies R. L., et al., 2001, *MNRAS*, 326, 23
- Baldwin J. A., Phillips M. M., Terlevich R., 1981, *Astronomical Society of the Pacific*, 93, 5
- Barden M., Rix H.-W., Somerville R. S., Bell E. F., Häußler B., Peng C. Y., Borch A., Beckwith S. V. W., et al., 2005, *ApJ*, 635, 959
- Beckman J. E., López-Corredoira M. N., Betancort-Rijo J., Castro-Rodríguez N., Cardwell A., 2003, *Astrophys. Space Sci.*, 284, 747
- Belley J., Roy J.-R., 1992, *Astrophysical Journal Supplement Series (ISSN 0067-0049)*, 78, 61
- Blanc G. A., Heiderman A., Gebhardt K., Evans N. J., Adams J., 2009, *ApJ*, 704, 842
- Boroson T., 1981, *ApJS*, 46, 177
- Briggs F. H., Wolfe A. M., Krumm N., Salpeter E. E., 1980, *ApJ*, 238, 510
- Bruzual G., Charlot S., 2003, *Mon. Not. R. Astron. Soc.*, 344, 1000
- Burstein D., Faber S. M., Gaskell C. M., Krumm N., 1984, *ApJ*, 287, 586
- Burstein D., Faber S. M., Gonzalez J. J., 1986, *Astronomical Journal (ISSN 0004-6256)*, 91, 1130
- Calzetti D., 1997, *Astronomical Journal v.113*, 113, 162
- , 2001, *PASP*, 113, 1449
- Cardelli J. A., Clayton G. C., Mathis J. S., 1989, *ApJ*, 345, 245
- Cardiel N., Gorgas J., Sánchez-Blázquez P., Cenarro A. J., Pedraz S., Bruzual G., Klement J., 2003, *A&A*, 409, 511
- Castellanos M., Díaz Á. I., Tenorio-Tagle G., 2002a, *ApJ*, 565, L79
- Castellanos M., Díaz A. I., Terlevich E., 2002b, *Mon. Not. R. Astron. Soc.*, 329, 315
- Cepa J., Beckman J. E., 1990, *Astrophysical Journal v.349*, 349, 497
- Chabrier G., 2003, *PASP*, 115, 763
- Charlot S., Fall S. M., 2000, *ApJ*, 539, 718
- Cornett R. H., O'Connell R. W., Greason M. R., Offenberg J. D., Angione R. J., Bohlin R. C., Cheng K. P., Roberts M. S., et al., 1994, *ApJ*, 426, 553
- Daigle O., Carignan C., Amram P., Hernandez O., Chemin L., Balkowski C., Kennicutt R., 2006, *Mon. Not. R. Astron. Soc.*, 367, 469
- de Zeeuw P. T., Bureau M., Emsellem E., Bacon R., Carollo

- C. M., Copin Y., Davies R. L., Kuntschner H., et al., 2002, *Mon. Not. R. Astron. Soc.*, 329, 513
- Deharveng J.-M., Jedrzejewski R., Crane P., Disney M. J., Rocca-Volmerange B., 1997, *A&A*, 326, 528
- Denicoló G., Terlevich R., Terlevich E., 2002, *MNRAS*, 330, 69
- Diaz A. I., 1994, 1. IAC-RGO Meeting: Violent star formation - from 30 Doradus to QSOs, 105
- Díaz A. I., Castellanos M., Terlevich E., García-Vargas M. L., 2000, *Mon. Not. R. Astron. Soc.*, 318, 462
- Díaz A. I., Pérez-Montero E., 2000, *Mon. Not. R. Astron. Soc.*, 312, 130
- Diaz A. I., Terlevich E., Pagel B. E. J., Vilchez J. M., Edmunds M. G., 1987, *MNRAS*, 226, 19
- Diaz A. I., Terlevich E., Vilchez J. M., Pagel B. E. J., Edmunds M. G., 1991, *MNRAS*, 253, 245
- Dopita M. A., Fischera J., Sutherland R. S., Kewley L. J., Leitherer C., Tuffs R. J., Popescu C. C., van Breugel W., et al., 2006, *ApJS*, 167, 177
- Dopita M. A., Kewley L. J., Heisler C. A., Sutherland R. S., 2000, *ApJ*, 542, 224
- Edmunds M. G., Pagel B. E. J., 1984, *MNRAS*, 211, 507
- Faber S. M., Friel E. D., Burstein D., Gaskell C. M., 1985, *Astrophysical Journal Supplement Series* (ISSN 0067-0049), 57, 711
- Fathi K., Beckman J. E., Zurita A., Relaño M., Knapen J. H., Daigle O., Hernandez O., Carignan C., 2007, *A&A*, 466, 905
- Ferguson A. M. N., Gallagher J. S., Wyse R. F. G., 1998, *AJ*, 116, 673
- Fernandes R. C., Mateus A., Sodr e L., Stasińska G., Gomes J. M., 2005, *MNRAS*, 358, 363
- Fukugita M., Shimasaku K., Ichikawa T., 1995, *PASP*, 107, 945
- Gadotti D. A., dos Anjos S., 2001, *AJ*, 122, 1298
- Ganda K., Falc n-Barroso J., Peletier R. F., Cappellari M., Emsellem E., McDermid R. M., de Zeeuw P. T., Carollo C. M., 2006, *Mon. Not. R. Astron. Soc.*, 367, 46
- Ganda K., Peletier R. F., McDermid R. M., Falc n-Barroso J., de Zeeuw P. T., Bacon R., Cappellari M., Davies R. L., et al., 2007, *Mon. Not. R. Astron. Soc.*, 380, 506
- Gil de Paz A. G., Boissier S., Madore B. F., Seibert M., Joe Y. H., Boselli A., Wyder T. K., Thilker D., et al., 2007a, *ApJS*, 173, 185
- Gil de Paz A. G., Madore B. F., Boissier S., Thilker D., Bianchi L., Contreras C. S., Barlow T. A., Conrow T., et al., 2007b, *ApJ*, 661, 115
- Gorgas J., Faber S. M., Burstein D., Gonzalez J. J., Courteau S., Prosser C., 1993, *Astrophysical Journal Supplement Series* (ISSN 0067-0049), 86, 153
- Hendry M. A., Smartt S. J., Maund J. R., Pastorello A., Zampieri L., Benetti S., Turatto M., Cappellari E., et al., 2005, *MNRAS*, 359, 906
- Holmberg E., 1975, *Galaxies and the Universe*. Edited by Allan Sandage, 123
- Hoopes C. G., Waltherbos R. A. M., Bothun G. D., 2001, *ApJ*, 559, 878
- Izotov Y. I., Stasińska G., Meynet G., Guseva N. G., Thuan T. X., 2006, *A&A*, 448, 955
- James P. A., Seigar M. S., 1999, *A&A*, 350, 791
- Jenkins E. B., 1987, *IN: Interstellar processes; Proceedings of the Symposium*, 134, 533
- Kamphuis J., Briggs F., 1992, *Astronomy and Astrophysics* (ISSN 0004-6361), 253, 335
- Kelz A., Verheijen M. A. W., Roth M. M., Bauer S. M., Becker T., Paschke J., Popow E., S nchez S. F., et al., 2006, *PASP*, 118, 129
- Kennicutt R. C., 1983, *ApJ*, 272, 54
- , 1998, *ARA&A*, 36, 189
- Kennicutt R. C., Armus L., Bendo G., Calzetti D., Dale D. A., Draine B. T., Engelbracht C. W., Gordon K. D., et al., 2003, *PASP*, 115, 928
- Kennicutt R. C., Garnett D. R., 1996, *ApJ*, 456, 504
- Kennicutt R. C., Hodge P. W., 1980, *ApJ*, 241, 573
- Kennicutt R. C., Lee J. C., Funes S. J., Sakai S., Akiyama S., 2008, *ApJS*, 178, 247
- Kewley L. J., Dopita M. A., 2002, *ApJS*, 142, 35
- Kewley L. J., Dopita M. A., Sutherland R. S., Heisler C. A., Trevena J., 2001, *ApJ*, 556, 121
- Kewley L. J., Ellison S. L., 2008, *ApJ*, 681, 1183
- Knapen, J. H., Beckman, J. E., Heller, C. H., Shlosman, I., & de Jong, R. S. 1995, *ApJ*, 454, 623
- Knapen J. H., Mazzuca L. M., B ker T., Shlosman I., Colina L., Combes F., Axon D. J., 2006, *A&A*, 448, 489
- Kobulnicky H. A., Kennicutt R. C., Pizagno J. L., 1999, *ApJ*, 514, 544
- Kobulnicky H. A., Kewley L. J., 2004, *ApJ*, 617, 240
- Koleva M., Prugniel P., Bouchard A., Wu Y., 2009, *A&A*, 501, 1269
- Kormendy J., Kennicutt R. C., 2004, *Annual Review of Astronomy & Astrophysics*, 42, 603
- Laine S., Shlosman I., Knapen J. H., Peletier R. F., 2002, *ApJ*, 567, 97
- Liang Y. C., Yin S. Y., Hammer F., Deng L. C., Flores H., Zhang B., 2006, *ApJ*, 652, 257
- L pez-Corredoira M., Betancort-Rijo J., Beckman J. E., 2002, *A&A*, 386, 169
- MacArthur L. A., Gonz lez J. J., Courteau S., 2009, *Mon. Not. R. Astron. Soc.*, 395, 28
- Marcum P. M., O'Connell R. W., Fanelli M. N., Cornett R. H., Waller W. H., Bohlin R. C., Neff S. G., Roberts M. S., et al., 2001, *ApJS*, 132, 129
- McCall M. L., Rybski P. M., Shields G. A., 1985, *ApJS*, 57, 1
- McGaugh S. S., 1991, *ApJ*, 380, 140
- Moustakas J., Kennicutt R. C., 2006a, *ApJ*, 651, 155
- , 2006b, *ApJS*, 164, 81
- Natali G., Pedichini F., Righini M., 1992, *Astronomy and Astrophysics* (ISSN 0004-6361), 256, 79
- Oconnell R. W., 1976, *ApJ*, 206, 370
- Ocvirk P., Pichon C., Lan on A., Thi baut E., 2006, *Mon. Not. R. Astron. Soc.*, 365, 46
- Osterbrock D. E., Ferland G. J., 2006, *Astrophysics of gaseous nebulae and active galactic nuclei*, University Science Books, Herndon VA, USA
- Pagel B. E. J., Edmunds M. G., Blackwell D. E., Chun M. S., Smith G., 1979, *MNRAS*, 189, 95
- Pagel B. E. J., Edmunds M. G., Smith G., 1980, *MNRAS*, 193, 219
- Peletier R. F., Balcells M., 1996, *Astronomical Journal* v.111, 111, 2238
- P rez-Montero E., D az A. I., 2005, *MNRAS*, 361, 1063
- Petersen L., Gammelgaard P., 1996, *A&A*, 308, 49
- Pettini M., Pagel B. E. J., 2004, *MNRAS*, 348, L59

- Pilyugin L. S., 2001, *A&A*, 374, 412  
 —, 2005, *A&A*, 436, L1  
 —, 2007, *Mon. Not. R. Astron. Soc.*, 375, 685  
 Pilyugin L. S., Contini T., Vílchez J. M., 2004, *A&A*, 423, 427  
 Pilyugin L. S., Thuan T. X., 2005, *ApJ*, 631, 231  
 Pilyugin L. S., Thuan T. X., Vílchez J. M., 2006, *Mon. Not. R. Astron. Soc.*, 367, 1139  
 Prescott M. K. M., Kennicutt R. C., Bendo G. J., Buckalew B. A., Calzetti D., Engelbracht C. W., Gordon K. D., Hollenbach D. J., et al., 2007, *ApJ*, 668, 182  
 Roberts M. S., 1962, *Astron. J.*, 67, 437  
 Rosales-Ortega F. F., Kennicutt R. C., Sanchez S. F., Diaz A. I., Pasquali A., Johnson B. D., Hao C. N., 2010, *arXiv*, 1002, 1946  
 Roth M. M., Kelz A., Fechner T., Hahn T., Bauer S.-M., Becker T., Böhm P., Christensen L., et al., 2005, *PASP*, 117, 620  
 Roy J.-R., Walsh J. R., 1988, *MNRAS*, 234, 977  
 Salpeter E. E., 1955, *ApJ*, 121, 161  
 Sánchez S. F., 2004, *AN*, 325, 167  
 —, 2006, *AN*, 327, 850  
 Sánchez S. F., Aceituno J., Thiele U., Pérez-Ramírez D., Alves J., 2007a, *PASP*, 119, 1186  
 Sánchez S. F., Becker T., García-Lorenzo B., Benn C. R., Christensen L., Kelz A., Jahnke K., Roth M. M., 2005, *A&A*, 429, L21  
 Sánchez S. F., Cardiel N., Verheijen M. A. W., Martín-Gordón D., Vílchez J. M., Alves J., 2007b, *A&A*, 465, 207  
 Sánchez S. F., Cardiel N., Verheijen M. A. W., Pedraz S., Covone G., 2007c, *Mon. Not. R. Astron. Soc.*, 376, 125  
 Sarzi M., Falcón-Barroso J., Davies R. L., Bacon R., Bureau M., Cappellari M., de Zeeuw P. T., Emsellem E., et al., 2006, *Mon. Not. R. Astron. Soc.*, 366, 1151  
 Scott P., Asplund M., Grevesse N., Sauval A. J., 2009, *ApJ*, 691, L119  
 Scowen P. A., Hester J. J., Gallagher J. S., Wilcots E., Idt T. W.-., 1996, *BAAS*, 189, 1360  
 Seigar M. S., 2002, *A&A*, 393, 499  
 Shostak G. S., van der Kruit P. C., 1984, *Astronomy and Astrophysics (ISSN 0004-6361)*, 132, 20  
 Serra, P., & Trager, S. C. 2007, *MNRAS*, 374, 769  
 Stasińska G., 2005, *A&A*, 434, 507  
 Stoklasová I., Ferruit P., Emsellem E., Jungwiert B., Pécontal E., Sánchez S. F., 2009, *A&A*, 500, 1287  
 Storchi-Bergmann T., Calzetti D., Kinney A. L., 1994, *ApJ*, 429, 572  
 Storey P. J., Zeppen C. J., 2000, *Mon. Not. R. Astron. Soc.*, 312, 813  
 Thomas D., Maraston C., Bender R., 2003, *Monthly Notice of the Royal Astronomical Society*, 339, 897  
 Thomas, D., Maraston, C., Bender, R., & Mendes de Oliveira, C. 2005, *ApJ*, 621, 673  
 Tinsley B. M., 1980, *FCPh*, 5, 287  
 Trager S. C., Dalcanton J., Marzke R. O., McWilliam A., Weiner B. J., 1998, *American Astronomical Society*, 193, 1331  
 van Zee L., Salzer J. J., Haynes M. P., O'Donoghue A. A., Balonek T. J., 1998, *AJ*, 116, 2805  
 Veilleux S., Osterbrock D. E., 1987, *Astrophysical Journal Supplement Series (ISSN 0067-0049)*, 63, 295  
 Verheijen M. A. W., Bershady M. A., Andersen D. R., Swaters R. A., Westfall K., Kelz A., Roth M. M., 2004, *AN*, 325, 151  
 Wakker B. P., Adler D. S., 1995, *The Astronomical Journal (ISSN 0004-6256)*, 109, 134  
 Worthey G., 1994, *ApJS*, 95, 107  
 Young J. S., Allen L., Kenney J. D. P., Lesser A., Rownd B., 1996, *Astronomical Journal v.112*, 112, 1903  
 Zaritsky D., Kennicutt R. C., Huchra J. P., 1994, *ApJ*, 420, 87

## APPENDIX A: MULTIPLE STELLAR POPULATION FITTING

A substantial fraction of the stellar continuum emission in early-type galaxies is dominated by a single-stellar population, reflecting the fact that their cosmological evolution is, in many cases, well described by a monolithic collapse model. In this scenario most of the star formation took place in these galaxies for a short time at early times, and therefore, their SFH can be well described by a single star-formation process. As a consequence, their stellar continuum can be easily described by a single-stellar population.

It is well known that the spectral energy distribution (SED) of simple stellar populations (chemically homogeneous and coeval stellar systems) depends on a set of first principles (e.g. initial mass function, star formation rate, stellar isochrones, metallicity, etc.), from which it is possible to generate the spectra of synthetic stellar populations. This technique, known as evolutionary synthesis modeling (e.g. Tinsley 1980), has been widely used to unveil the stellar population content of galaxies by reconciling the observed spectral energy distributions with those predicted by the theoretical framework. Unfortunately the variation of different physical quantities governing the evolution of stellar populations produce similar effects in the integrated light of those systems, leading to a situation in which the observational data is affected by undesirable degeneracies, like the widely mentioned one between age and metallicity (e.g. Oconnell 1976; Aaronson et al. 1978; Worthey 1994). However, the use of spectrophotometrically calibrated spectra and the sampling of a wide wavelength range, as in the present data set, helps to break the degeneracy and allows the derivation reliable physical parameters by fitting the full spectral distribution with single-stellar populations (Cardiel et al. 2003).

However, the simple assumption that a single-stellar population describes well the SED of a galaxy is not valid for late-type galaxies. These objects present complex star formation histories, with different episodes of activity, of variable intensity and time scale. Therefore, a single-stellar population does not reproduce well their stellar emission, in general terms. A different technique, known as full-spectrum modeling, involving the linear combination of multiple stellar populations and the non-linear effects of dust attenuation, has been developed to reconstruct their stellar populations (e.g. Fernandes et al. 2005; Ocvirk et al. 2006; Sarzi et al. 2006; Koleva et al. 2009; MacArthur et al. 2009).

In general, these reconstructions require a wide wavelength range to probe the hot, young stars and the cool,

old stars simultaneously. They also require the best spectrophotometric calibration to disentangle the effects of age, metallicity and dust attenuation. Although different implementations of this technique have some differences, they are very similar in their basis, as described above. The extracted information from the multi stellar-population modelling differs in the different implementations. In some cases the luminosity (or mass) weight ages and metallicities are derived, based on the linear combination of different models (e.g. Sarzi et al. 2006). In other implementations the fraction of light (or mass) of different stellar populations (e.g. Stoklasová et al. 2009), or the fraction of light (or mass) that corresponds to old or young stellar populations (e.g. MacArthur et al. 2009) are derived.

For our particular analysis, it is necessary to model accurately the underlying continuum not only to understand the nature of the stellar population, but also to obtain a good representation of the continuum in order to decouple it from the emission lines produced by the ionized gas. Therefore, even in the case that the combination of SSPs is strongly degenerate, and the created model has no physical meaning, it could be partially useful for our purposes.

The implementation of the multi stellar-population fitting technique used in this article is part of the FIT3D package (e.g. Sánchez et al. 2007b,c), and it has been recently used by (e.g. Stoklasová et al. 2009) in the analysis of the stellar population of nearby galaxies based on IFS data. This package enables linear fits of a combination of SSPs, and non-linear ones of emission-lines plus an underlying stellar population. It also includes routines to extract the 2D distribution of the different derived parameters based on the analysis of the stellar population (age, metallicity, dust) and/or the analysis of the emission lines (flux intensity, systemic velocity and velocity dispersion). The package will be delivered to the public in a forthcoming paper. The basic steps of the fitting algorithm, spectrum by spectrum, are the following:

(i) Read the input spectrum, determine the areas to be masked, and construct the variance map. Lets define  $G_i$  as the observed galaxy flux at wavelength  $\lambda_i$ , and  $N$  the number of elements of the masked spectrum.

(ii) Read the set of SSP template spectra, shift them to the systemic velocity of the considered spectrum, convolve them to match its spectral resolution and velocity dispersion, and resample them to its wavelength solution. Lets define  $F_{ji}$  as the flux of the  $i^{th}$  wavelength of the  $j^{th}$  template (once shifted, convolved and resampled), where  $M_0$  is the total number of considered templates.

(iii) Apply a certain dust attenuation to the templates. The attenuation law of Cardelli, Clayton & Mathis (1989) was adopted, with a ratio of total to selective attenuation of  $R_V = 3.1$  (Jenkins 1987). Lets define  $F_{ji}^{A_V}$  as the flux of the  $i^{th}$  wavelength of the  $j^{th}$  template, after applying the dust attenuation corresponding to a certain attenuation of  $A_V$  magnitudes.

(iv) Perform a linear least-square fitting of the input spectrum with the set of SSP templates, using a modified  $\chi^2$  as a merit function to be minimised, with the form:

$$\chi^2 = \frac{1}{N - M} \sum_{i=1}^N R_i^2,$$

where

$$R_i = w_i \left( G_i - \sum_{j=1}^M a_j F_{ji}^{A_V} \right),$$

In the above expression,  $w_i$  is the weight of the  $i^{th}$  pixel, defined as

$$w_i = \frac{1}{\sigma_i^2},$$

and  $a_j$  is the coefficient of the  $j^{th}$  template in the final modelled spectrum, and  $M$  is the number of templates considered in the fitting procedure.

(v) Determine for which templates the fitting procedure produces negative coefficients in the linear combination (i.e.  $a_j < 0$ ). These templates will be excluded from the next iteration of the fitting procedure, that will be resumed in the step (iii). At each iteration,  $M$  is decreased by the amount of excluded templates. This loop ends once all the coefficients are positive.

(vi) The modified  $\chi^2$  corresponding to the considered dust attenuation is stored as  $\chi_{A_V}^2$ , and the fitting procedure is repeated again starting at the step (iii), modifying the considered amount of dust and starting the procedure with the full set of templates (i.e.  $M = M_0$ , again). This loop ends once the dust attenuation has covered a pre-defined range of possible values, that it is defined as an input parameter.

(vii) The best linear combination of templates and dust attenuations are selected based on the minimization of the stored  $\chi^2$  parameters. The final modelled spectrum flux at  $\lambda_i$  is given by

$$S_i = \sum_{j=1}^M a_j F_{ji}^{A_V},$$

where in this case, only the  $M$  templates with positive coefficients  $a_j$  are considered, and  $A_V$  corresponds to that value which minimises  $\chi_{A_V}^2$ .

(viii) The luminosity-weighted age ( $H$ ) and metallicity ( $Z$ ) of the underlying stellar population is then derived by the formulae:

$$H = \sum_{j=1}^M a_j H_j,$$

and

$$Z = \sum_{j=1}^M a_j Z_j,$$

where  $H_j$  and  $Z_j$  are the corresponding age and metallicity of the  $j^{th}$  SSP template. These luminosity-weighted ages and metallicities should be considered as the *luminosity-weighted* ages and metallicities of the modeled stellar popula-

**Figure A1.** Spectra of the 72 SSP templates used in the population synthesis fits. Metallicity increases from the top-left to the bottom-right. Different ages are represented by different colours. All the spectra are normalized to the flux at 5000 Å.

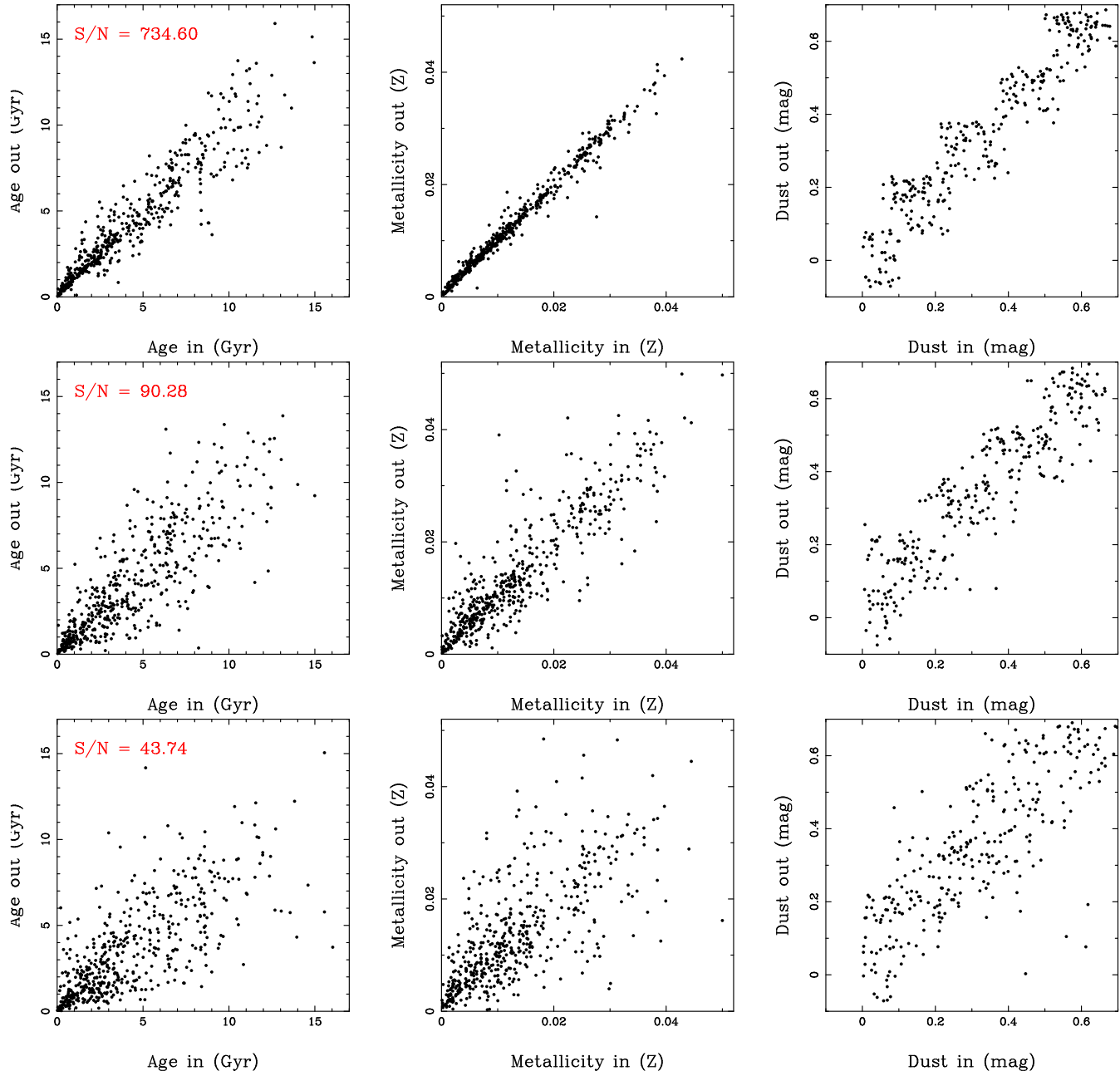


**Figure A2.** Results from the simulations. Each panel shows, from left to right, the comparison between the input luminosity-weighted age, metallicity and dust attenuation, with the recovered values by our fitting technique. The results are presented for different signal-to-noise ratios, decreasing from the upper to the lower panels. A random value of  $\pm 0.08$  mag has been added to output attenuation to show all the values, since they are originally quantized to steps of 0.1 mag.

tion, since they would match with the corresponding values if the population was composed by a single SSP.

This algorithm shares a basis with many other procedures described in the literature (e.g. Fernandes et al. 2005, Sarzi et al. 2006, MacArthur et al. 2008). If required, low-frequencies in the spectrum can be fitted by adding to the fitted templates a polynomial function, or by multiplying them by that function. There are different origins for these

low-frequencies in the spectrum, mostly related with defects in the reduction process. In the particular case of the data analyzed in the current article, the inclusion of this additional step in the fitting procedure does not improve considerably the results.

By construction, the fitting algorithm is useful for masking undesirable regions in the spectrum. In general, it is needed to mask: (i) strong and variable night sky-line re-

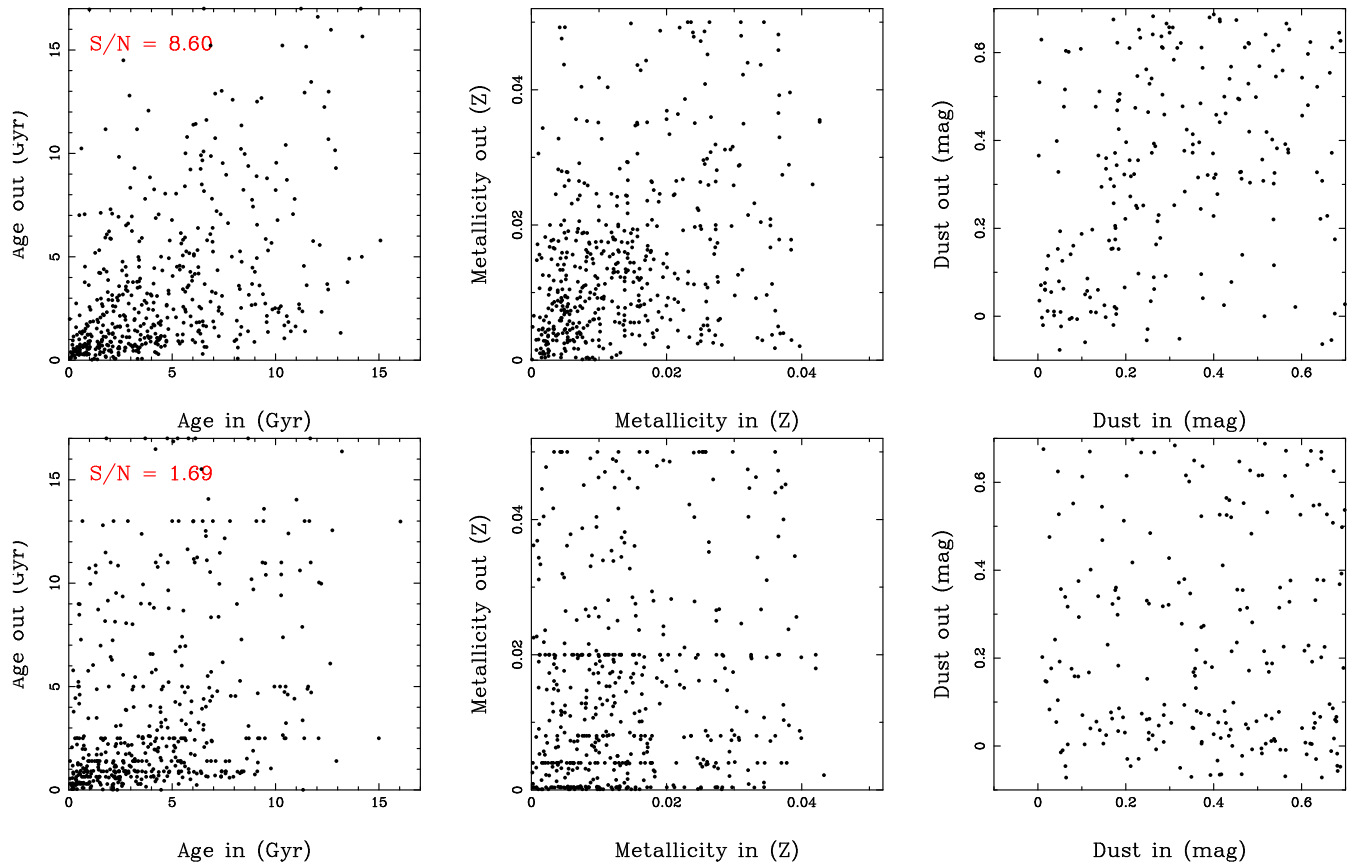


Figure A2. Continue

gions, (ii) regions affected by defects in the CCD (like dead columns) whose effect was not completely removed during the data reduction process, (iii) regions affected by telluric absorption, not completely corrected during the flux calibration process, and (iv) regions containing emission lines from ionized gas.

As indicated above, one of the main goals of this fitting procedure is to provide with an accurate modelling of the underlying stellar population, and to derive a pure-emission line spectrum, given by

$$C_i = G_i - S_i.$$

### A1 Modelling the emission lines

To derive the intensity of each detected emission line, the *clean* spectrum ( $C_i$ ) is fitted to a single Gaussian function per emission line plus a low order polynomial function. This fit is performed using non-linear fitting routines implemented in FIT3D, that were described in previous articles. Instead of fitting all the wavelength range in a row, we extracted for each spectrum shorter wavelength ranges that sampled one or a few of the analysed emission lines, in order to characterise the residual continuum with the most simple polynomial function, and to simplify the fitting procedure. When more than one emission was fitted simultaneously, their systemic velocities and FWHMs were forced to be equal (since the FWHM is dominated by the spectral

resolution), in order to decrease the number of free parameters and increase the accuracy of the deblending process (when required). These procedures are frequently used, and therefore, we will not explain them in more detail.

A modelled gas-emission spectrum is created, based on the results of the last fitting procedure, using only the combination of Gaussian functions. This spectrum is given by

$$E_i = \sum_{k=1}^L B_k * GAUSS_{ik}(\lambda_k, \sigma_k),$$

where  $L$  is the number of emission lines considered in the model,  $B_k$  is the integrated flux of the  $k^{th}$  emission line, and  $GAUSS_{ik}$  is the corresponding normalized Gaussian function (with central wavelength  $\lambda_k$ , and dispersion  $\sigma_k$ ), evaluated at the  $i^{th}$  pixel.

Finally, the original spectrum ( $G_i$ ) is decontaminated by the gas emission, subtracting this modeled gas-emission spectrum, deriving a gas-free spectrum given by

$$GF_i = G_i - E_i.$$

This spectrum is then used to model the stellar population, by applying the procedure described before, but without masking the emission lines spectral regions. We adopted the results from this second iteration as a better modeling of the stellar population.

## A2 SSP template library

As noted by MacArthur et al. (2009), this kind of analysis is always limited by the template library, which comprises a discrete sampling of the SSP ages and metallicities. It would be desired for the stellar library to be as complete as possible, and non-redundant. However, this would require an exact match between the models and the data, which is not possible to achieve in general terms, in particular if the stellar population comprises more than one SSP. As a suitable solution for the analysis presented in this article, we adopted a SSP template library that covers the widest possible range of ages and metallicities. This template has already been demonstrated as useful for modelling the stellar population of a varied set of galaxies (see Sánchez et al. 2007c).

The SSP models were created using the GISSEL code (Bruzual & Charlot 2003), assuming a Salpeter IMF (Salpeter 1955) (the use of Chabrier 2003, will not modify the results), for different ages and metallicities. We create 72 models covering a discrete grid of 12 ages (5 Myr, 25 Myr, 100 Myr, 290 Myr, 640 Myr, 0.9 Gyr, 1.4 Gyr, 2.5 Gyr, 5 Gyr, 11 Gyr, 13 Gyr, and 17 Gyr), and 6 metallicities ( $Z = 0.0001, 0.0004, 0.004, 0.008, 0.02$  and  $0.05$ ). Figure A1 shows the spectra of all the templates, grouped by their metallicity, and normalized to their flux at  $5000 \text{ \AA}$ . The adopted library is similar in many respects to the one proposed by MacArthur et al. (2009). Both libraries have a similar number of templates, although the latter library has a wider coverage of the ages and a more reduced coverage of the metallicities of the stellar populations.

There is a number of caveats when applying model SSPs to the integrated light of a star forming galaxy, which have been clearly identified by MacArthur et al. (2009). The most important one is to assume that the parameter space covered by the empirical library represents well that of the real data. However in general, libraries are based on stars in the solar neighborhood, and therefore it is not granted that they represent well the stellar populations in other galaxies (or even in other regions of our Galaxy). There are other potential problems related to the particular selected templates, since it is well known that the Bruzual& Charlot (2003) models have problems when dealing with the non-solar abundance ratios. Most of these problems are not particularly important in the context of our science case, since (i) our primary goal is to model the stellar population to analyse the ionized gas emission and (ii) we are interested in relative assessments about the nature of the stellar populations in different regions of the studied galaxy, and not in absolute values.

In addition, it is important to note that the treatment of the dust attenuation may affect the resulting derived parameters (i.e. the luminosity-weighted age and metallicity of the stellar population). In this particular implementation of the analysis we adopted the Cardelli et al. (1989) attenuation law, which may not be the optimal solution to study the dust attenuation in star-forming galaxies (e.g. Calzetti 2001). MacArthur et al. (2009) adopted a completely different attenuation law, based on the two-components dust model of Charlot & Fall (2000), which is particularly developed to model the dust attenuation in star forming galaxies. Despite the conceptual differences between the two attenuation laws, their actual shapes are very similar in the wavelength range covered by our data. The final range of dust

**Table A1.** Results of the simulations.

S/N	rms	$\Delta\text{Age}/\text{Age}$	$\Delta Z$	$\Delta A_V$
734.60	0.14	$0.02 \pm 0.14$	$0.0001 \pm 0.0014$	$0.00 \pm 0.05$
90.28	0.11	$-0.03 \pm 0.24$	$0.0006 \pm 0.0047$	$0.01 \pm 0.08$
43.74	0.11	$-0.08 \pm 0.30$	$0.0004 \pm 0.0074$	$0.03 \pm 0.13$
8.60	0.12	$-0.18 \pm 0.46$	$0.0014 \pm 0.0126$	$0.04 \pm 0.38$
1.69	0.12	$-0.18 \pm 0.59$	$0.0006 \pm 0.0164$	$-0.06 \pm 0.51$
*82.77	0.12	$0.21 \pm 0.27$	$0.0010 \pm 0.0070$	$-0.01 \pm 0.10$
**81.97	0.13	$0.12 \pm 0.47$	$0.0023 \pm 0.0075$	$-0.01 \pm 0.23$

\* Results when fitting the simulated spectra with a different library of SSPs than the one used to create the simulation.

\*\* Results when the input simulated spectra consists of a single SSP, instead of a combination of them.

attenuations explored by our fitting technique comprises  $A_V$  values up to 1 mag, with steps of 0.1 mag.

## A3 Accuracy of the derived parameters

As mentioned before, the basic parameters derived by the analysis of the stellar component are the *luminosity-weighted* age, metallicity and dust attenuation of the composite stellar population. In order to assess the accuracy of these parameters we have performed a set of simulations. The simulations were performed while trying to match as closely as possible the original data, especially the noise pattern, which is composed of both white noise corresponding to the photon-noise of the source and the background, and electronic noise from the detector; and non-white noise corresponding to defects/inaccuracies in the sky-subtraction, uncorrected defects in the CCD, etc. These noise patterns are different spectrum-to-spectrum, and wavelength-to-wavelength, and are clearly difficult to simulate on a simple analytical basis.

Five different sets of simulations were performed. In each one, 500 simulated spectra were created with the same normalized flux at  $5000 \text{ \AA}$ , corresponding to 100, 10, 5, 1 and  $0.2 \cdot 10^{-16} \text{ erg s}^{-1} \text{ cm}^{-2} \text{ \AA}^{-1}$ , respectively. For each simulation, a composite stellar population was considered, comprising 4 different SSP extracted randomly from the considered library template, with a different relative contribution each one to the total flux: 53%, 27%, 13% and 6% at  $5000 \text{ \AA}$ , respectively. This procedure was adopted to resemble in a simple way a possible star-forming history, with a dominant stellar population, and three different bursts or merging events. Different experiments adopting a larger number of intermix stellar populations, and relative contributions of each one to the total were considered, with no significant variations on the derived conclusions.

Once a particular spectrum was created, it was convolved with the instrumental resolution of the observed data, and the corresponding noise pattern was added. The noise pattern was created on the basis of the residuals of the fitting procedure applied over the observational data. For each spectrum of the original mosaic, the fitting procedure creates a residual spectrum, once the derived composite stellar population and emission line models were subtracted. This *noise* spectrum includes all the effects of the white noise (for

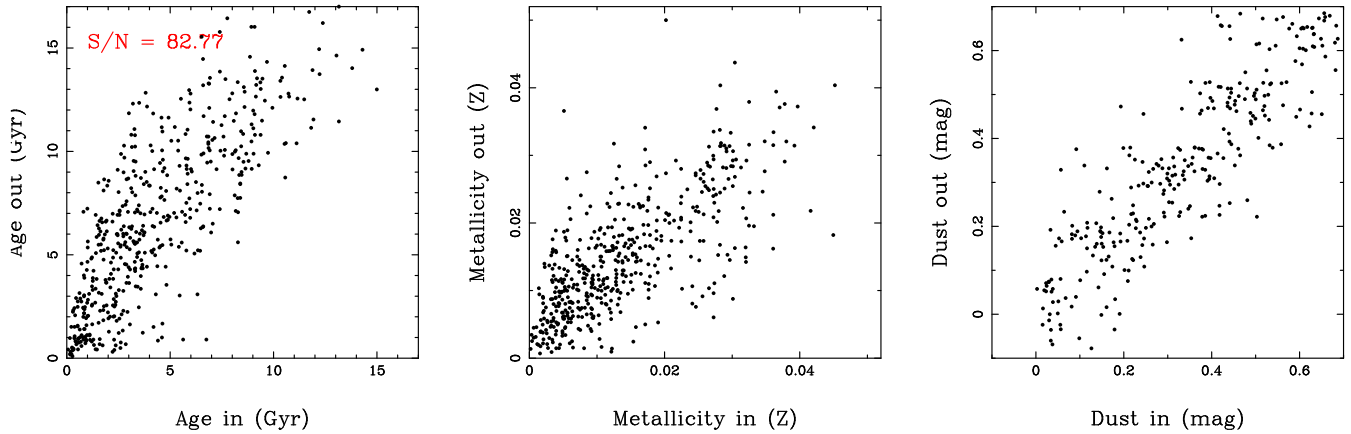


**Figure A3.** Results from the simulations. Each panel shows, from left to right, the comparison between the input luminosity-weighted age, metallicity and dust attenuation, with the recovered values by our fitting technique. The difference from Fig. A2 is that in this particular case, a different library of SSPs was adopted to fit the spectra, compared to the one used to simulate them, as described in the text.

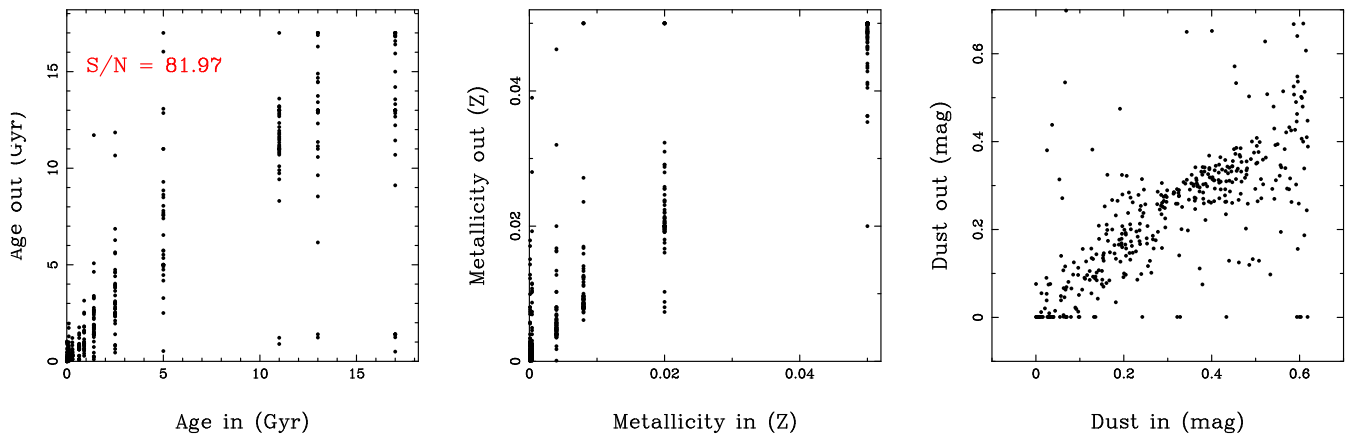


**Figure A4.** Results from the simulations. Each panel shows, from left to right, the comparison between the input luminosity-weighted age, metallicity and dust attenuation, with the recovered values by our fitting technique. The difference from Fig. A2 is that in this particular case, the input model consists of a single SSPs, although it is fitted following the prescriptions shown in the text.

a particular flux level), and non-white noise (deficient sky subtraction, CCD defects not corrected by the reduction, imperfections of the modelling process, etc.). From this set of *noise* spectra, one was randomly selected for each simulated spectrum, fulfilling the requirement that the simulated and original fluxes at  $\sim 5000 \text{ \AA}$  match within a range of  $\sim 20\%$ . The selected *noise* spectrum was then added to the simulated spectrum.

The fitting procedure was then applied to the simulated spectra using the same steps adopted to analyse the observational data, deriving, for each one, the *luminosity-weighted* ages, metallicities and dust attenuation, and a new residual spectrum. Table A1 lists, for each set of simulated spectra, their average signal-to-noise ratio, the *rms* of the relative difference between the input spectra (without noise) and the model derived by the fitting procedure and the difference between the input and the recovered parameters that define these models (luminosity-weighted age, metallicity and dust attenuation), and their corresponding *rms*. As expected the parameters are better recovered for the spectra with higher signal-to-noise ratios, requiring at least a S/N of  $\sim 50$  per pixel to derive accurate results. Figure A2 illustrates these

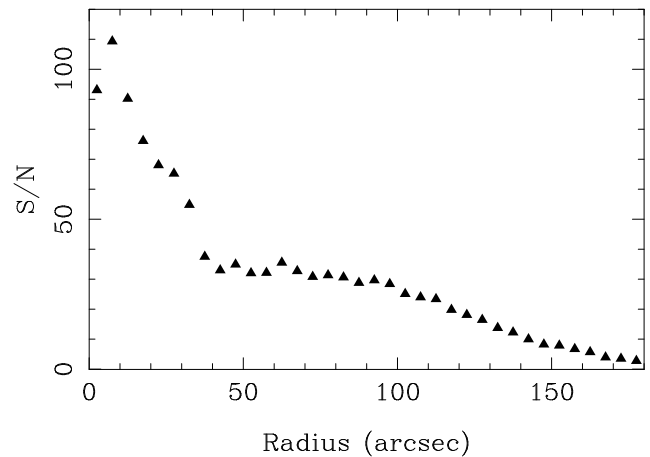


**Figure A5.** Radial distribution of the average S/N at  $\sim 5000 \text{ \AA}$  of the spectra within the flux calibrated mosaic of NGC 628.

results, showing for each set of simulations the comparison between the input and recovered parameters for each individual spectrum in the dataset.

A possible source of error in the interpretation of these simulations is the fact that the same set of templates was used to create the simulated data and to model them. In principle, we assumed that the grid of templates is representative of the real stellar population of the analysed spectra, but it is very possible that our library is incomplete. This is not the case in our simulations, by construction. To study the effects of this possible incomplete representation of the observational spectra by the template library, we created a new set of simulated data, corresponding to a flux level of  $10 \cdot 10^{-16} \text{ erg s}^{-1} \text{ cm}^{-2} \text{ \AA}^{-1}$ , that was then fitted using a much reduced version of the template library. This template comprises a grid of 12 SSPs, corresponding to 3 ages (17 Gyrs, 900 Myrs and 25 Myrs), and 4 metallicities ( $Z = 0.0001, 0.004, 0.02, 0.05$ ). The results from this simulation are listed in Table A3, and shown in Figure A3. It shows that in the case of an incomplete coverage of the spectroscopic parameters by the model template, these parameters are still well reconstructed, albeit with a lower accuracy (as expected).

Finally, we tested how well the code is able to reproduce a pure SSP, instead of a mixture of them. With this test we try to overpass the intrinsic problems in the interpretation of the luminosity-weighted ages/metallicities in galaxies, and to test if we can recover the better understood properties of a pure single-burst population. The results from this simulation are listed in Table A3, and shown in Figure A4. Despite the discrete coverage of the input parameters, it is clear that the parameters are recovered just slightly worse than in the case of a multiple component stellar population.

On the other hand, the relative difference between the original spectra and the recovered model is lower than  $\sim 15\%$  for all the simulations, even in those ones for which the accuracy of the recovered parameters is deficient. These differences are of just 2-3% for the spectra with the highest signal-to-noise ( $>100$ ). This basically means that the general shape of the spectra is better recovered than the parameters that defines them. This is easy to understand, since these parameters are characterised by particular features in the spectra, rather than by their general shapes, which are more degenerated.

Figure A5 shows the radial distribution of the average signal-to-noise ratio at  $\sim 5000 \text{ \AA}$  of the spectra within the flux-calibrated mosaic of NGC 628, as described in Sec. 3. On the basis of this radial profile and the results of the simulations discussed before it is possible to recover the considered parameters of the composite stellar populations for individual spectra only at radii less than  $\sim 10 \text{ arcsec}$ , for the central kpc of the galaxy. The results are robust only for the integrated spectrum of the galaxy (with a  $S/N \sim 400$ ), and for radii lower than  $\sim 20 \text{ arcsec}$  (with  $S/N \sim 100$ ). However, for the azimuthally averaged spectra, where the signal-to-noise increases by the root-mean square of the number of individual averaged spectra, the simulations indicate that the recovery of the considered parameters is robust even at radii as large as  $\sim 120 \text{ arcsec}$ , above which both the  $S/N$  and the number of spectra with accurate spectrophotometry also drops (see Figure 4). The combination of both effects impose a limitation to the accuracy of the derived parameters at higher radii.